Surface Energy in Bond-Counting Models on Bravais and Non-Bravais Lattices

A Dissertation Presented for the

Doctor of Philosophy

Degree

The University of Tennessee, Knoxville

Tim Ryan Krumwiede

May 2017

© by Tim Ryan Krumwiede, 2017
All Rights Reserved.

Abstract

Continuum models in computational material science require the choice of a surface energy function, based on properties of the material of interest. This work shows how to use atomistic bond-counting models and crystal geometry to inform this choice as well as to make predictions regarding dendritic growth behavior in bond-counting models. We will examine some of the difficulties that arise in the comparison between these models due to differing types of truncation. New crystal geometry methods are required when considering materials with non-Bravais lattice structure, resulting in a multi-valued surface energy. These methods will then be presented in the context of the two-dimensional material graphene in a way that correctly predicts its equilibrium shape.

Table of Contents

1 Introduction **1**

2 Preliminary Information **3**

2.1 Lattices . . . 3

2.1.1 2-Dimensional Lattices . . . 4

2.1.2 3-Dimensional Lattices . . . 5

2.2 Kinetic Monte Carlo Models . . . 6

2.2.1 Computational Considerations . . . 10

3 Dendritic Growth Shapes in Bravais Lattice Models **16**

3.1 Introduction . . . 16

3.2 Kinetic Monte-Carlo . . . 18

3.2.1 KMC Simulation of Dendritic Growth . . . 20

3.3 Surface Energy in Bond-Counting Models . . . 22

3.4 Equilibrium and Growth Shape . . . 26

3.5 Discussion and Conclusion . . . 29

4 Graphene Edge Energy **35**

4.1 Edge Energy Calculation . . . 37

4.1.1 Bravais Refined Lattice . . . 39

4.1.2 Uniform Edges . . . 40

4.1.3 Funny Edges . . . 42

4.1.4 Non-Commensurate Edges 46
4.2 Generalization for All Graphene Bonds 47
4.3 Comparison with Graphene Literature 49
4.4 KMC Experimentation 50
4.5 Conclusion 53

5 More Non-Bravais Lattice Examples **54**
5.1 Bravais Alloys 54
5.2 The Hexagonal Close-Packed Lattice 57

6 Conclusion **59**

Bibliography **61**

Vita **64**

List of Figures

2.1 Two examples of 2-dimensional Bravais lattices. 4

2.2 The triangular lattice is the only 2-dimensional Bravais lattice with six nearest-neighbor directions. The graphene lattice is not Bravais as there are two sets of neighbor directions differentiated by A and B atoms in this figure. 5

2.3 The graphene lattice is a lattice with a basis consisting of two atoms copied over a Bravais lattice. 6

2.4 The face-centered cubic lattice with unit primitive vectors, which can be constructed as layers of the 2D triangular lattice. 7

2.5 The hexagonal close-packed lattice. Like FCC, this lattice can also be constructed with sheets of the triangular lattice, but is not Bravais. Atoms in the top and bottom sheets shown here have nearest neighbors in directions that differ from those of the middle layer. 7

2.6 The selected atom in this 2D example has two neighbors and four unoccupied neighbor sites. Its hopping rate is then $R_a = 4\exp\left(-2/(k_bT)\right)$. 9

3.1 An illustration of the simulation domain, nucleated growth species in the center, and adatoms diffusing through the far-field. 21

3.2 An illustration in two dimensions of a Bravais lattice, its two primitive vectors, a single bond corresponding to $\mathbf{v}$, a facet with normal $\hat{\mathbf{n}}$, and the collection of bond-facet intersections. The latter forms Bravais lattice in one fewer dimensions along the facet. 23

3.3 A 2D illustration of an arbitrary bond and a prismatic primitive cell with base parallel to a facet with normal $\hat{\mathbf{n}}$. In this case the Voronoi cell of facet intersections consists of a line segment and is shaded in the figure. 25
3.4 Examples of Surface Energies 26
3.5 A 2-dimensional example of the Wulff construction using the edge energy function of nearest-neighbor bonds on the regular triangular lattice. 27
3.6 KMC simulations of an FCC crystal's equilibrium shape under two different temperatures, with energy scaled such that $w_1 = 0.1$ eV. Higher temperatures lead to softer edges as seen in b. 28
3.7 FCC Wulff shapes and the corresponding results of a KMC simulation on a FCC lattice. The Wulff shapes in a & b correspond to the surface energies in Fig. 3.4b and c, which are both on a FCC lattice. The dendrite shown in c & d use the same parameters as the Wulff shapes in a & b respectively. These crystals each contain approximately 5×10^6 atoms, with the inset showing an atomic resolution close-up. 29
3.8 Kinetic Monte-Carlo simulation using the value $w_2 = 0.353553$, which has been chosen to eliminate ϵ_1 in the cubic harmonic expansion of the surface energy (3.13). This dendrite contains approximately 5 million atoms. Note that there are 24 primary branches (six groups of four) that seem to be merging into six larger branches. 32
3.9 Wulff shapes corresponding to two surface energy functions. The first (a) corresponds to $\gamma_c(\hat{n}) = 1 - 0.02K_2(\hat{n})$. The second (b) corresponds to the FCC bond-counting model with $w_1 = 1$, $w_2 = 0.353553$ and has the cubic harmonic expansion $\gamma_b(\hat{n}) = 1 - 0.02K_2(\hat{n}) + \cdots$. 33
3.10 Wulff shape corresponding to surface energy $\gamma(\hat{\mathbf{n}}) = 1 - 0.02K_2 - 0.0150347K_3$. 34

4.1 In (a), we see two edges with the same normal $\hat{n} = (-1/2, \sqrt{3}/2)$ that also share the edge energy $\gamma(\hat{n}) = 2/3$. Any edge with this same normal will also have that same edge energy. However, in (b), two edges are shown with normal $\hat{n} = (1, 0)$ and yet have different energies. These are the only two edge energy values exhibited by edges with this normal. 36
4.2 An example of an edge and its sequence α. 38
4.3 The construction of the graphene lattice's corresponding Bravais refined lattice. 40
4.4 Here the bond intersections on one period of a uniform edge are illustrated. 41
4.5 Results of equilibrium KMC simulation on a hexagonal lattice. In (a), atoms are initially arranged as a hexagon with armchair orientation edges. In (b), the crystal seeks zigzag edges very quickly and eventually achieves a hexagonal shape in (d) with fully zigzag orientation edges. 42
4.6 Here the bond intersections on one period of a funny edge is illustrated. 43
4.7 Energy bands for two different funny edge orientations. The edges in (a) have normal $\hat{\mathbf{n}} = (-\sqrt{3}/2, 1/2)$ and the edges in (b) have normal $\hat{\mathbf{n}} = \left(-\frac{3}{2\sqrt{2}}, \frac{5}{2\sqrt{7}}\right)$. 44
4.8 A graph of γ^- in blue and γ^+ in gold is shown in (a). In (b), we show the result of the Wulff construction using γ^-. 45
4.9 Next-nearest-neighbor bonds occur between atoms of the same type. . 47
4.10 Next-next- and next-next-next-nearest neighbor bonds. Next-next-nearest-neighbor bonds shown in (a) do occur between A-type and B-type atoms, but they are in the same direction as nearest-neighbor bonds. Next-next-next-nearest-neighbor bonds with $\mathbf{v} = (\sqrt{3}, 2)$ are shown in (b). 48
4.11 The edge energy function of Liu et al. is shown in red and overlaid on the plot of funny edge energies γ. 51

4.12 Two 2-dimensional KMC simulations with reflective boundary conditions yielding equilibrium shapes. The top row is the time evolution of a flake of material with triangular lattice structure. The bottom row is that of a graphene flake, rotated so that both simulations have identically oriented equilibrium shapes. s is the number of KMC iterations. 52

5.1 An example of a three-species Bravais alloy on the regular triangular lattice. Each species, differentiated by red, yellow and blue nodes, is arrayed in a coarser Bravais lattice. The bonds between each pair of species have a different bond strength indicated by color: orange, green and purple. 55

5.2 The Bravais refined lattice corresponding to the HCP lattice. 58

Chapter 1

Introduction

Surface energy is defined as the difference between the total energy of a crystal and the energy within the interior of the crystal. This difference is a result of the fact that interior atoms are fully bonded and surface atoms have open bonds yielding a higher energy value. Surface energy is an important attribute of a crystal growth model. Some models require the choice of a surface energy function in terms of facet orientation, or edge energy for two-dimensional models, at the onset to determine the crystal's growth behavior. Other models may not require this choice, but still surface energy can be calculated and utilized to predict growth, as will be demonstrated in this work.

In a crystal bond-counting model, the potential energy depends only on the number of bonds in a system in which each atom can have a small number of bonds with nearby atoms. This is a huge simplification compared to a model with an empirical potential in which all atoms interact with every other atom in the system, but it is important for computability when modelling large atomic systems.

A crystal is any solid which assumes a periodic lattice structure at the atomic level. This includes not only what we colloquially refer to as crystal, but also most metals and ice. The lattice structure of a crystal encourages the use of a discrete lattice as a domain for our model. I will examine the use of two classifications of lattices

in the calculation and use of surface energy: Bravais and non-Bravais, to be defined later. The computation of surface energy for Bravais lattice models is straightforward and has been understood for a while, but I will demonstrate its utility in exploring growth behavior. For non-Bravais lattice models, however, surface energy is much more interesting and I will offer a thorough picture of the calculation of energy for graphene which assumes a non-Bravais lattice structure.

Chapter 2

Preliminary Information

2.1 Lattices

All of the models considered in this work are defined on a discrete lattice. In this section I will review some of the information on lattices that will be utilized throughout the rest of the sections.

Definition 1. *An n-dimensional Bravais lattice is defined as one in which every node is given by some integer combination of the vectors of a basis in* $\mathbb{R}^n$*. The vectors comprising this basis are referred to as primitive vectors.*

Bravais lattices are well understood and all Bravais lattices in $\mathbb{R}^2$ and $\mathbb{R}^3$ have been identified and classified. A property of Bravais lattices that we will take full advantage of is that the entire lattice is identical when viewed from the perspective of any lattice node. In other words, after translating the entire lattice in the direction of an integer combination of the primitive vectors, the result is identical to the original lattice. The primitive cell of a 2-dimensional Bravais lattice is defined as the parallelogram with the lattice primitive vectors as sides. The area of the primitive cell is given by $\det A$ where the columns of A are the primitive vectors of the lattice.

2.1.1 2-Dimensional Lattices

A 2-dimensional Bravais lattice is defined by a set of two linearly dependent vectors. The simplest example is the regular square lattice with primitive vectors $\{(1,0),(0,1)\}$ shown in Fig. 2.1a. Any two-dimensional Bravais lattice is a linear transformation of the regular square lattice by skewing, rotating and/or scaling as shown in 2.1b.

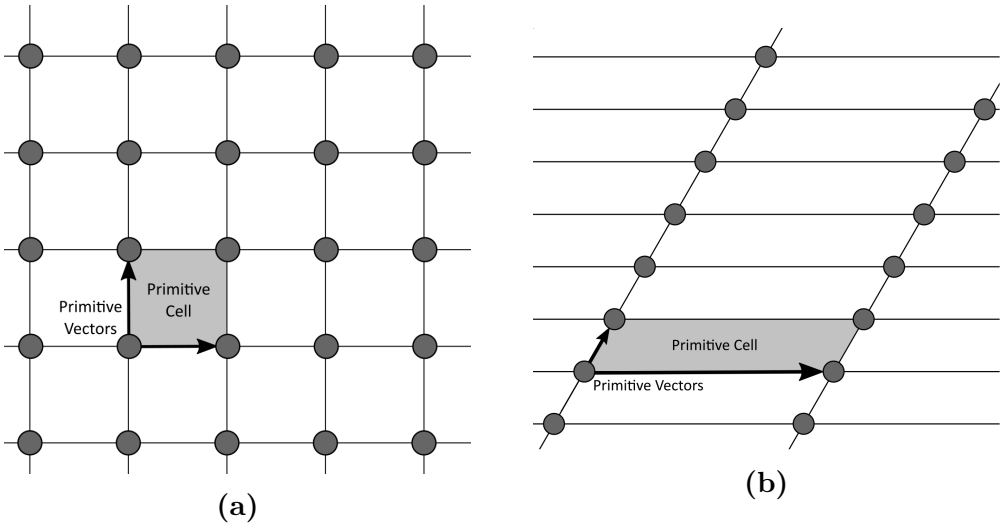


Figure 2.1: Two examples of 2-dimensional Bravais lattices.

An interesting example of a 2-dimensional Bravais lattice is the regular triangular lattice (also called the hexagonal or penny-packing lattice) defined by primitive vectors $\{\mathbf{a}_1 = (\sqrt{3}/2, 1/2), \mathbf{a}_2 = (0,1)\}$. Note that the $|\mathbf{a}_1 - \mathbf{a}_2| = 1$, meaning that each node has an additional two nearest neighbors compared to the square lattice.

Non-Bravais lattices form a much more broad and interesting class of lattices. In crystallography, a crystal lattice is considered a "lattice with a basis" if it can be constructed by translating copies of a bounded set of nodes at each node of some Bravais lattice. The 2-Dimensional example used extensively in Chapter 2 is the graphene lattice. It is not Bravais because some nodes have nearest neighbors in directions $\{(\pm\sqrt{3}/2, 1/2), (0,1)\}$ while other nodes have neighbors in directions $\{(\pm\sqrt{3}/2, -1/2), (0,-1)\}$. It is, however, a lattice with a basis because the graphene

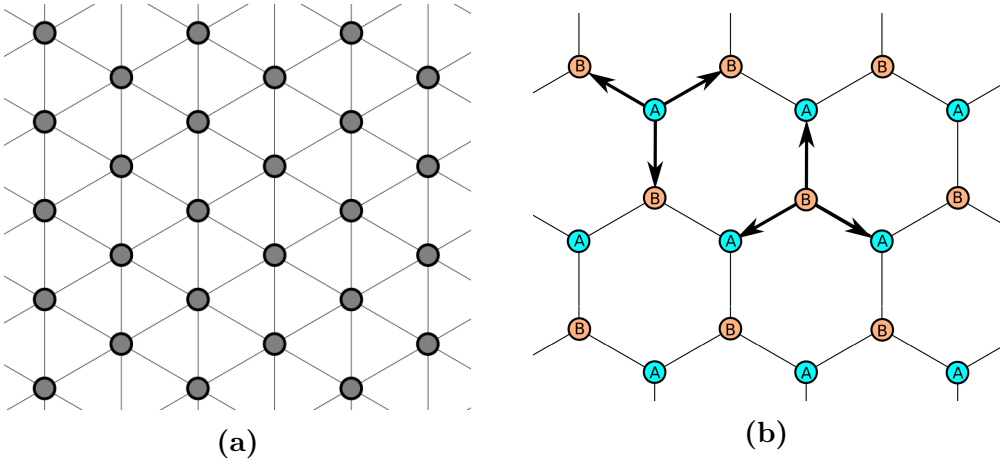


Figure 2.2: The triangular lattice is the only 2-dimensional Bravais lattice with six nearest-neighbor directions. The graphene lattice is not Bravais as there are two sets of neighbor directions differentiated by A and B atoms in this figure.

lattice can be constructed by translating a copy of a node and one of its neighbors on the Bravais lattice with primitive vectors $\{(\sqrt{3}, 0), (\sqrt{3}/2, 3/2\}$ as shown in Fig. 2.3.

2.1.2 3-Dimensional Lattices

Similarly, the simplest 3-Dimensional lattice is the simple cubic lattice with primitive vectors $\{(1, 0, 0), (0, 1, 0), (0, 0, 1)\}$ and any 3-D Bravais lattice is a linear transformation of this lattice. One of the most common 3-Dimensional Bravais lattices seen in nature is the face-centered cubic (FCC) lattice shown in Fig. 2.4 with primitive vectors the edges of a regular tetrahedron: $\{(1, 0, 0), (1/2, \sqrt{3}/2), (1/2, 1/\sqrt{12}, \sqrt{2/3})\}$. This lattice can be visualized as layers of the regular triangular lattice offset so as to give each node twelve nearest neighbors: six in its own layer, three in the layer above and three in the layer below. In every fourth layer, the nodes lie directly above the nodes of the first.

The hexagonally close-packed (HCP) lattice is non-Bravais but closely related to the FCC lattice. HCP again consists of layers of the triangular lattice offset to give each node twelve nearest neighbors but rather than use the same vector to generate the third layer, nodes in the third layer lie directly above the first layer

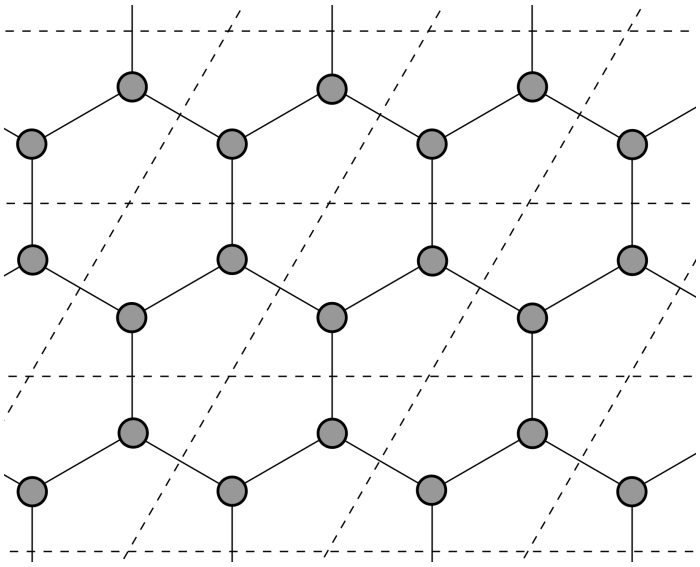


Figure 2.3: The graphene lattice is a lattice with a basis consisting of two atoms copied over a Bravais lattice.

as in Fig. 2.5. This results in a lattice with a basis where the basis consists of two nodes $\{(0,0,0),(1/2,1/\sqrt{12},\sqrt{2/3})\}$ copied on the lattice with primitive vectors $\{(1,0,0),(1/2,\sqrt{3}/2),(0,0,2\sqrt{2/3})\}$.

2.2 Kinetic Monte Carlo Models

A Monte Carlo method is any mathematical algorithm that utilize series of random samplings to obtain results. They have been studied for centuries, though it is only with the advent of modern computing that they have truly become useful and interesting. A dynamic Monte Carlo model is one in which a system evolves randomly in time. A Kinetic Monte Carlo model is specifically an atomistic material model in which one atom is randomly selected and moves each iteration.

Monte Carlo models are not the most accurate of atomistic models. Other models such as molecular dynamics and density functional theory are much more detailed in terms of interactions between atoms and assume interactions between all particles in the system. KMC models sacrifice much of this detail in favor computability, by using

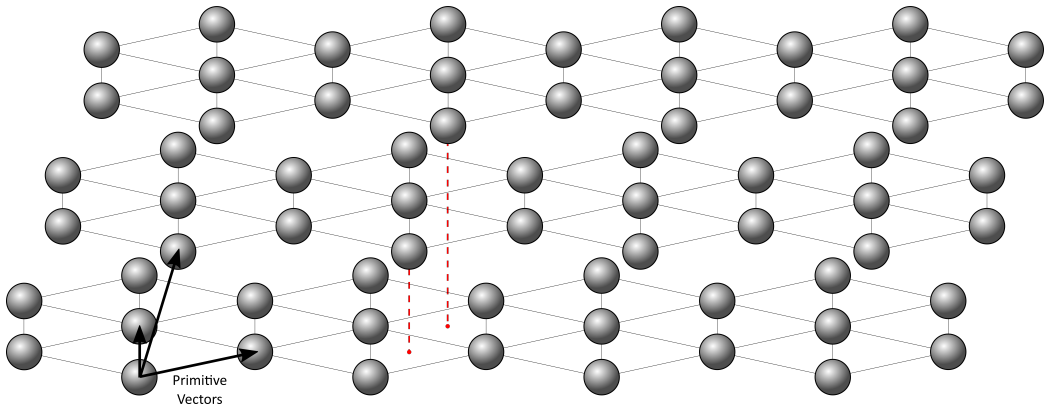


Figure 2.4: The face-centered cubic lattice with unit primitive vectors, which can be constructed as layers of the 2D triangular lattice.

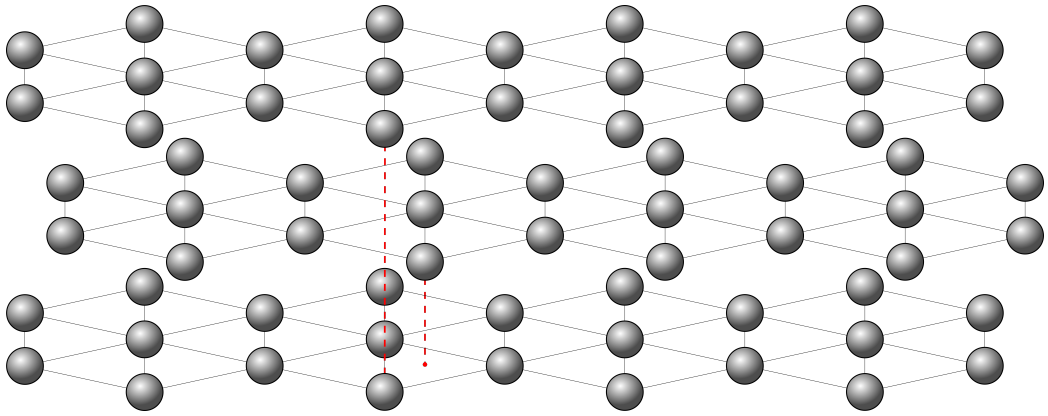


Figure 2.5: The hexagonal close-packed lattice. Like FCC, this lattice can also be constructed with sheets of the triangular lattice, but is not Bravais. Atoms in the top and bottom sheets shown here have nearest neighbors in directions that differ from those of the middle layer.

simple pair potential interactions and only between an atom and its near neighbors which drastically simplifies the model's state-space. The computability gains are significant and KMC can be used for much larger systems and broader time scales than molecular dynamics and other atomistic models.

On the other hand, macroscale simulations are usually done with continuum techniques such as phase-field modelling. These models drop atomistic interactions altogether and instead seek a time evolution of crystal growth by solving a system of PDEs to determine a curve/manifold that represents the crystal surface. These

models are widely studied but it is not clear in the literature how the accuracy of these models is affected by the exclusion of atomistic effects.

In this work, I will focus on the study of on-lattice KMC in which all atoms occur at the discrete nodes of a periodic lattice running through the domain. For example, the face-centered cubic or FCC lattice is the result of placing a new node on each face of a unit cell in the simple cubic lattice in $\mathbb{R}^3$. This is a useful lattice for materials science modelling, as many metals solidify with an FCC lattice structure. Within this structure, each atom has 12 nearest neighbors and 6 next-nearest neighbors.

A KMC simulation on an FCC lattice records for each atom the number of nearest-neighbor nodes also occupied by an atom. This is then used to determine the atoms probability of hopping to an open neighboring node. The hopping rate of an atom to one of its open neighbor nodes is given by

$$R = K \exp\left(-\frac{E - E_T}{k_b T}\right)$$

where E is the system energy, E_T is the energy of a transition state, k_b is the Boltzmann constant, T is a constant temperature term, and K is a normalizing constant. The transition state is defined as the current state without the moving atom and any bonds it shares. By summing up over the possible hop events for a particular atom, we see that its total movement rate is

$$R_a = (12 - N_a) \exp\left(-\frac{N_a}{k_b T}\right)$$

where $N_a \in \{0, 1, 2, \ldots, 12\}$ is the number of neighbors of atom a. Therefore, the hopping rate of an atom in this model solely depends on its number of neighbors as shown in Fig. 2.6.

The rates for all atoms in the system are summed up for a total rate which can be used to normalize the rates and construct a discrete probability distribution. This distribution is used to select the movement event and the selected atom is moved to

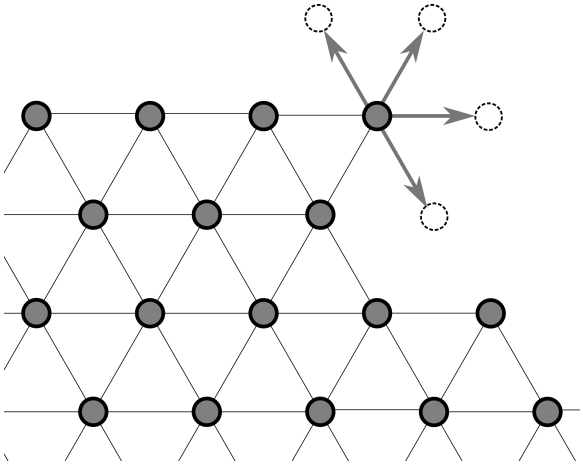


Figure 2.6: The selected atom in this 2D example has two neighbors and four unoccupied neighbor sites. Its hopping rate is then $R_a = 4\exp(-2/(k_b T))$.

one of its unoccupied neighbor sites. At each iteration of the simulation, an atom moves which changes the rates of neighboring atoms as well. Thus the probability distribution changes at each step as well. This model is then a Markov process that transitions between configurations at each iteration, and each iteration's distribution can be represented by a sparse transition matrix.

As mentioned earlier, KMC models time evolution of crystals and generally only for cold temperatures. An atom in the system moves at every iteration but in the physical scenario, this will not occur at uniform time increments. Thus, we model the passage of time as a Poisson process. Time is updated at the end of each simulation step by picking a random number r in $(0, 1)$ and setting

$$T = T + \ln(1/r)/P$$

where $P = \sum_a R_a$.

However, if we are only interested in the qualitative behavior of the system being simulated, we may not need to track simulation time at all. In this case, in the interest of optimizing speed, it's worth omitting this calculation altogether.

2.2.1 Computational Considerations

A basic KMC code is not overly difficult to write. However, some measures must be taken if the simulation is optimized to the point that systems containing millions of atoms can be simulated for a sufficient amount of time. However, with such large systems, it can be easy to rely too much on computer memory and overload RAM. A successful KMC program optimizes speed without significant memory redundancy.

Data Structures

In order to optimize execution speed, several large data structures must be used. These data structures require some intensive bookkeeping as well, and I provide the details here. All the code used as part of this work has been programmed in Fortran 95, which has the benefits of running very quickly (especially in a Linux environment) and easy management of data structures. I will refer to specific data structures in this section using the same name I've used in the code and written in italics.

Many of the structures used in my KMC code are paired with associated inverse arrays. For example, two of the primary arrays are *state* and *atomlist*. The domain is represented by *state*, which in the FCC KMC simulation is a three-dimensional array such that every lattice node within the model domain is represented by an entry in *state*. One way to assign the required geometry to *state* is to let the *state* location with index (i, j, k) correspond to the lattice node given by $+i\mathbf{v}_1 + j\mathbf{v}_2 + k\mathbf{v}_3$ where $\mathbf{v}_1, \mathbf{v}_2$, and $\mathbf{v}_3$ are the primitive vectors of the FCC lattice. This is a straightforward choice because the FCC lattice is Bravais. The entries of *state* take integer values with positive integers indicating an occupied node, 0 indicating an unoccupied node, and negative integers indicating any nodes that are outside of the domain boundaries.

The inverse data structure of *state* is *atomlist*. *atomlist* has three columns and enough rows so as to never overflow throughout the simulation. Every atom's *state* coordinates are stored in the three entries of the row corresponding to that atom so calling *atomlist*$(a,:)$ returns the location of the atom corresponding to row a which will

be referred to as the atom number. Also, the value of *state* at an occupied node is equal to the atom number a of the occupying atom. These two structures are considered inverses because $state(atomlist(a,:)) = a$ and $atomlist(state(i,j,k)) = (i,j,k)$.

Another primary data structure is called *list*. *list* is important in the selection of the moving atom and is analagous to sorting events by event label as described by Schulze (2008a). When using the FCC lattice, it is a 2-dimensional array with 12 rows (sorted by coordination number from 0 to 11) and enough columns to fit a large portion of the maximum number of particles. The rows are indexed from 0 to 11 and within each row are the atom numbers of atoms with the same number of neighbors, referred to as the atom's coordination number. It is possible to write a KMC code without the use of a *list* array. However, it allows us to first select the coordination number of the moving atom and then select a random atom from the corresponding *list* row. The use of *list* is a necessary part of ensuring that the mode;'s computational cost is independent of system size.

It is not necessary to store atoms with twelve neighbors in a *list* row since these atoms have no unoccupied neighbor nodes and therefore can't move. This saves a good deal of memory associated with list especially in a crystal growth simulation because most atoms will have 12 neighbors. This decision does require extra care in terms of bookkeeping, though, since fully coordinated atoms can become 11-neighbor atoms when a neighbor moves, and need to be introduced back into *list* row 11.

Atoms change coordination numbers as they or their neighbors move, so we need a way to find where a particular atom appears in *list* to be able to keep it updated. This requires an inverse array called *inv_list* which returns the coordination number and spot in the corresponding *list* row for atom a. Both *list* and *inv_list* need to be updated for each atom affected by any move. Also, as part of this selection scheme, we must keep track of the number of atoms within each *list* row in a small array I call *census*.

Reduction of Random Number Generation

We can exploit the discreteness of this model in order to minimize the number of random number generations per step. Anytime a random number chosen from an interval is used to select an event from a finite set, we can extract a new random variable from the difference rather than generating a new one. For example, consider the algorithm for selecting the event type at the beginning of each iteration:

1. Calculate partial sums given by $P_j = \sum_{i=0}^{j} rates(i) \cdot census(j)$ for $j = 0, ..., 11$.
2. Let $P = P_{11} + genrate$ where *genrate* is the atom generation rate at the boundary.
3. Randomly generate a number r in $(0, P)$.
4. Compare r to P_j.
    - If $r > P_{11}$, a new atom will generate at the boundary during the current iteration.
    - If $P_{j-1} < r \leq P_j$, an atom with coordination number j will move during the current iteration.
5. Randomly select one of the atoms with coordination j using *list*.

This algorithm requires two random variables. Of course we can generate a new random number each time, but if this code is to be run for trillions of iterations it loses a significant amount of efficiency. A more efficient method involves using the difference $r - P_{j-1}$, which is a uniform random variable on the interval $(0, P_j - P_{j-1}]$, as the second random number to select either the atom to move or the generation site to use. If moving an atom, this overshot technique can be used again to select the moving atoms new site from the list of unoccupied neighbor nodes. This technique does have its limitations due to finite precision and can thus only be used a few times per step.

Local Updates

A naive approach to programming an on-lattice KMC model might involve counting bonds for each atom in the system at each step in order to find the hopping rates. This is extremely computationally intensive for large systems but is also completely unnecessary. Because each move only affects the rates of the moving atom, its neighbors before moving, and its neighbors after moving, we can store neighbor counts in a data structure and only update these lists for the affected atoms during each step.

This can be easily managed within the process of moving an atom:

1. Once the moving atom is selected, check each neighboring site for occupancy.
    - If occupied, decrease the neighbor's neighbor count in *inv_list* by one and move the neighbor to the correct column in *list*.
    - If unoccupied, record this direction in the temporary array *movedir* as a potential move direction.
2. Pick a new site for the moving atom at random using *movedir*.
3. After moving, check each new neighboring site for occupancy.
    - If occupied, increase the neighbor's neighbor count in *inv_list* by one and move the neighbor to the correct column in*list*.

When done correctly, the selected atom has moved to an unoccupied neighbor site and all of the affected data structures are updated.

Equilibrium Shape Variation

The model described thus far has flux at the boundary, since new atoms are generated on the boundary and diffusive atoms that move past the boundary are terminated. This leads to crystal growth behavior and for certain parameters yields a dendritic growth shape. We can change the boundary conditions to reflect atoms at the

boundary instead, which would model a crystal in equilibrium and converge to the crystal's equilibrium shape. Perhaps the simplest way to implement this change is to simply reject any move outside of the domain boundary and move on to the next iteration.

The Full Algorithm

Initialization:

1. Set necessary parameters (domain size, temperature, generation rate, max particles).
2. Build *state* array.
3. Place atoms within a small radius of the center of the domain by building *atomlist* and updating *state*.
4. Build *list*, *inv_list* and *census* by counting neighbors for each atom.
5. Calculate rates for each coordination number using the given temperature and store in *rates*.

Iteration:

1. Calculate partial sums of the entries of *census* and the generation rate and let the total be P.
2. Randomly generate a number r in $(0, P)$.
3. Compare r to the partial sums to select the coordination number of the moving atom, or to generate a new atom at the boundary.
4. If moving an existing atom:
   (a) Use the overshot of r to pick a random atom from the corresponding *list* row.

(b) Follow Local Updates algorithm to move the selected atom and update data structures. Use overshot of r again to randomly pick the atoms direction.

(c) Check to see if the atom is leaving the domain. If so, terminate and update the data structures.

5. If generating a new atom:

   (a) Use the overshot of r to select a boundary node.

   (b) Generate a new atom at the boundary node. Update data structures accordingly.

6. Update simulation time.

Chapter 3

Dendritic Growth Shapes in Bravais Lattice Models

3.1 Introduction

Dendritic growth has been studied extensively from both an experimental and theoretical point of view. This intense study is due to fundamental scientific interest as well as the importance of this striking phenomenon from a technological point of view. The vast majority of dendrite simulations have used continuum models aimed at macroscale solid-liquid interfaces, e.g. a pure solid growing into its melt. In this work, I seek to build upon the smaller body of work that has examined dendritic growth on atomistic length scales using KMC simulation. These models are best suited to growth from vapor with low concentrations of the growth species. Interfaces where a solid is in equilibrium with its melt tend to be at much higher temperature and pressure than interfaces where a vapor is in equilibrium with a solid. Thus, our simulations correspond to lower temperatures, with a correspondingly lower entropic contribution to the surface free energy and crystal surfaces that tend to be more faceted.

While the growth of a snowflake is a familiar example of this regime, KMC studies have tended to focus on more idealized systems, most often the growth of simple cubic crystals. These studies include the work of Witten and Sander on diffusion limited aggregation (Witten and Sander, 1981). To simulate more structured dendritic growth one must include a surface diffusion mechanism. For simple cubic growth, this has been examined in a number of two-dimensional studies (Vicsek, 1984; O. Shochet and Muller-Krumbhaar, 1992; Harris and Grant, 1990; Saito and Ueta, 1989), and at least one study of three-dimensional growth (L. Jorgenson and Guo, 1993).

More recently, Schulze (2008b) has examined KMC simulation of FCC dendrites. This model aims to examine the growth of a dendrite into an under-cooled melt using a hybrid KMC-continuum model where the thermal diffusion was simulated using the heat equation discretized on the FCC lattice. From the nanoscale perspective, this has the disadvantage of removing thermal fluctuations from the model. In contrast, our present work will consider instead the growth of a dendrite from a super-saturated vapor, modeled as a lattice gas at constant temperature. The bulk diffusion of the precipitating species is then readily simulated with a random walk, so that the fluctuations in the growth process can be more consistently modeled.

The aim here is to examine a broader class of KMC models capable of capturing a wider range of dendrite morphology. This was initially motivated by the work of T. Haxhimali and Rappaz (2006) who have pointed out that the vast majority of work using continuum models has been aimed at the growth of FCC and other cubic dendrites with primary growth occurring along the six faces of the cubic unit cell. In particular, their work emphasizes the potential for moving continuously from $\langle 100 \rangle$- to $\langle 110 \rangle$-oriented growth as one varies composition-dependent surface energy parameters. According to their model, this would result in a transition from six- to twelve-armed dendrites with a variety of complicated and fascinating hybrid structures in between.

T. Haxhimali and Rappaz (2006) base their conclusions on phase field simulations of a continuum model with a truncated expansion of the anisotropy in the interfacial

free-energy, $\gamma(\theta, \phi)$, in terms of "cubic harmonics", K_1 and K_2, which are formed from linear combinations of spherical harmonics $Y_{lm}(\theta, \phi)$ to reflect the symmetry of cubic crystals:

$$\gamma(\theta, \phi) \approx \gamma_0[1 + \epsilon_1 K_1(\theta, \phi) + \epsilon_2 K_2(\theta, \phi)]. \tag{3.1}$$

The coefficients, ϵ_1 and ϵ_2, are material-dependent anisotropy parameters. The authors note that essentially all prior studies retain only the $\epsilon_1 K_1$-term that favors the ubiquitous $\langle 100 \rangle$ dendrite, and point to an earlier Molecular Dynamics (MD) study of J.J. Hoyt and Karma (2003) that suggests the $\epsilon_2 K_2$-term, which favors $\langle 110 \rangle$-oriented growth, is significant for a wide range of FCC metals. They support their theory with both simulations of the continuum model for dendritic growth into an under-cooled melt and directional solidification experiments of $Al - Zn$ alloys. The experiments study the surface energy anisotropy by considering varying amounts of Zn, and support the numerical study. We seek a similar generalization for KMC studies of crystal growth aimed at the nanoscale.

In the next section we start with a more general and formal approach to KMC than the previous chapter before turning to the specific model used for the present study. In Section 3 we derive the surface energy for our model, and in Section 4 we examine the corresponding equilibrium shapes as well as the growth shapes that emerge as the result of simulation. In Section 5 we discuss the relationship with the work of Haxhimali et al. and some important distinctions between the continuum and KMC models.

3.2 Kinetic Monte-Carlo

KMC models usually take the form of discrete-space, continuous-time Markov processes, where the system passes through a sequence of states $\{\mathbf{x}_{\alpha_n} \in \mathcal{X}\}$ drawn from a model dependent state-space $\mathcal{X} = \{\mathbf{x}_\alpha = \{x_{ijk} \in \{0, 1\}\}\}$ at transition times $\{t_n\}$. Here α is a discrete index used to enumerate the possible states. The states

themselves, $\mathbf{x}_\alpha$, take the form of an occupation array for some set of lattice points, with 1 signifying occupied and 0 unoccupied. In this paper, for example, we consider an arbitrary Bravais lattice $\{i\mathbf{a}_1 + j\mathbf{a}_2 + k\mathbf{a}_3\}$ defined by a set of primitive vectors $\{\mathbf{a}_1, \mathbf{a}_2, \mathbf{a}_3\}$.

In KMC, the transition matrix for the Markov process is typically sparse, with rates $R_{\alpha\beta} = 0$ except for certain local transitions. In this paper, we consider models that are mostly limited to the exchange of neighboring occupied and unoccupied lattice sites. In other words, every transition on the interior of the domain consists of a single atom moving to an unoccupied site. The transition rates $R_{\alpha\beta}$ are chosen so that an equilibrium simulation will achieve the Boltzmann distribution:

$$\rho(\mathbf{x}) = Z^{-1} \exp\left(-\frac{E(\mathbf{x})}{k_b T}\right), \quad Z = \sum_{x \in \mathcal{X}} \exp\left(-\frac{E(\mathbf{x})}{k_b T}\right), \tag{3.2}$$

where $\rho(\mathbf{x})$ is the probability of finding the system in state $\mathbf{x}$, $E(\mathbf{x})$ is a discrete Hamiltonian associating an energy with each possible state, Z is the canonical partition function, k_b is the Boltzmann constant, and T is the temperature, which we take to be uniform across the system.

A simple and conventional way of enforcing the correct equilibrium distribution in (3.2) is to impose a condition of *detailed balance*:

$$\rho(\mathbf{x}_\alpha) R_{\alpha\beta} = \rho(\mathbf{x}_\beta) R_{\beta\alpha}, \tag{3.3}$$

which matches the flux between any two states. A common choice for the rates $R_{\alpha,\beta}$ that satisfies (3.3) and that is motivated by Transition State Theory (Voter, 2007) is

$$R_{\alpha\beta} = K \exp\left(-\frac{E(\mathbf{x}_\alpha) - E_{\alpha\beta}}{k_b T}\right), \tag{3.4}$$

where the prefactor K is normally taken to be a constant and $E_{\alpha\beta}$ is the energy of the "transition state". In a model based on an empirical potential, where particles

can occupy an arbitrary point in configuration space, the transition state is identified with the energy at saddle points on the energy landscape. In a lattice-based model, there are no such points and we simply define $E_{\alpha\beta}$ to play an analogous role. In many bond-counting models, including those considered here, $E_{\alpha\beta}$ can be thought of as the energy of the system with the transitioning atom removed. Equivalently, the energy barrier $E(\mathbf{x}_\alpha) - E_{\alpha\beta}$ is defined to be the interaction energy between the atom being moved and the rest of the system.

3.2.1 KMC Simulation of Dendritic Growth

For the present simulations, we imagine a vapor solution initially at a uniform concentration and a temperature that will remain constant. The domain is a sphere of fixed radius, large enough that this concentration may be assumed fixed at the boundary of the sphere. The precipitate is nucleated in a much smaller sphere at the center of the domain (see Fig. 3.1). Growth occurs as particles precipitate and diffuse along the surface of the crystal, which depletes the concentration of the solidifying species in a boundary layer that conforms to the crystal surface. This depletion of the precipitating species provides the driving force for the morphological instability, as protruding portions of the surface have access to a richer concentration of the growth species in the far-field.

More specifically, these simulations use a large FCC lattice within a spherical domain with a radius of approximately 200 lattice spacings. An occupied lattice site represents an atom of the growth species, whereas an empty site represents the solution from which the dendrite is growing. The diffusion of the growth species from the far-field to the crystal surface is modeled as a random walk on an FCC lattice with subsequent attachment and surface diffusion. An alternative model with an off-lattice random walk was also considered, but rejected in favor of the more readily implemented discrete model. Initially, all nodes within five lattice spacings from the center are considered occupied, constructing a small cluster with about 600 atoms.

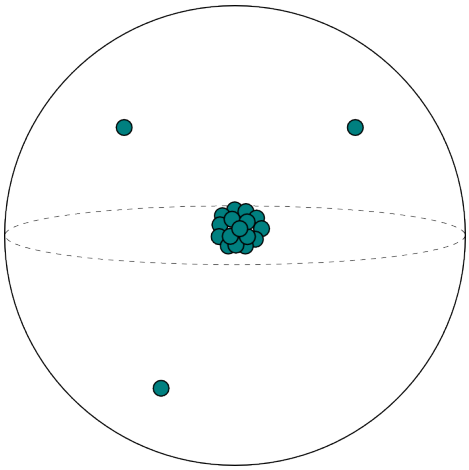


Figure 3.1: An illustration of the simulation domain, nucleated growth species in the center, and adatoms diffusing through the far-field.

In principle, each atom shares interactions with all other atoms in the system. However, in our simulations, interactions are limited to a finite number of pairwise "bonds." Since every node in a Bravais lattice has neighbors in the same directions, each bond can be represented by a vector between nodes of the lattice: $\mathbf{v} = v_1\mathbf{a}_1 + v_2\mathbf{a}_2 + v_3\mathbf{a}_3$ with $v_i \in \mathbb{Z}$. Without loss of generality, we will arbitrarily associate these bonds with one of the two interacting atoms by choosing an orientation for $\mathbf{v}$, and denote the set of bonds for a given model as $\{\mathbf{v}_j\}$.

The energy $E(\mathbf{x})$ is given by

$$E(\mathbf{x}) = -\frac{1}{2}\sum_{i=1}^{n_a}\sum_{j=1}^{n_b} w_j N_j(i), \tag{3.5}$$

where n_a is the number of atoms, n_b is the number of bond types $\{\mathbf{v}_j\}$, w_j is the weight corresponding to $\mathbf{v}_j$ or the energy value of a $\mathbf{v}_j$ bond, and $N_j \in \{0, 1, 2\}$ is the number of bonds an atom shares with its neighbors with either $\mathbf{v}_j$ or $-\mathbf{v}_j$ orientation.

The transition rate $R_{\alpha\beta}$ for the surface diffusion process depends solely on how many bonds it shares with neighbors. The rate for an atom moving to an open site

is given by

$$R = K \exp\left(-\frac{1}{k_b T} \sum_{j=1}^{n_b} w_j N_j\right).$$

In the models we will consider, many of the bonds share the same weight.

At each iteration of the simulation either a single atom moves to an adjacent site on the lattice or a new atom is generated on the domain boundary. The rates for the single atom moves are a function of the number of occupied nearest- and next-nearest-neighbor sites denoted $R_{n_1 n_2}$. Additionally, we need a counter $a_{n_1 n_2}$ telling us the number of events with rate $R_{n_1 n_2}$ in the current configuration. Finally, there is one additional rate g representing the uniform flux of the growth species from the far-field.

These simulations are performed with two different boundary conditions. When growing a dendrite, atoms are deposited onto boundary sites at a uniform rate and annihilated upon moving onto a boundary site, so that a uniform far-field concentration is maintained. When finding equilibrium shapes, all flux at the boundary is removed by setting $g = 0$ and reflecting atoms that move onto a boundary site, so that the number of atoms n_a is conserved.

3.3 Surface Energy in Bond-Counting Models

To gain insight into the equilibrium behavior of the bond-counting model just described, we first derive the corresponding surface energy function, $\gamma_b(\hat{\mathbf{n}})$, which we define as the number of broken bonds per unit area along a surface with normal $\hat{\mathbf{n}}$. Note that, in contrast to (3.1) this is a zero-temperature surface energy rather than a free-energy. In the KMC simulations, the entropic effects due to finite temperature are controlled via the rates (3.4), whereas in a continuum model they are modeled through the choice of γ, e.g. (3.1). Derivation of the surface energy function of bond-counting models for FCC metals has been demonstrated in previous studies for bonds up to a specified truncation radius (J.K. Mackenzie and Nicholas, 1962; Y. Luo, 2014;

Herring, 1951). I offer an alternative derivation for surface energies of models on any Bravais lattice with an arbitrary set of bonds of any length.

We calculate the total surface energy for a facet with normal $\hat{\mathbf{n}}$ by computing the contribution of each $\mathbf{v} \in \{\mathbf{v}_j\}$ individually. A 2D example of this is shown in Fig. 3.2, along with a facet cutting bonds associated with the same vector $\mathbf{v}$. It's important to note that, depending on the length of $\mathbf{v}$, bonds between atoms may overlap. This happens if and only if $z \equiv \gcd(v_1, v_2, v_3) > 1$, since the bond given by $\mathbf{v}$ crosses that many atoms (this is also the density of overlapping bonds).

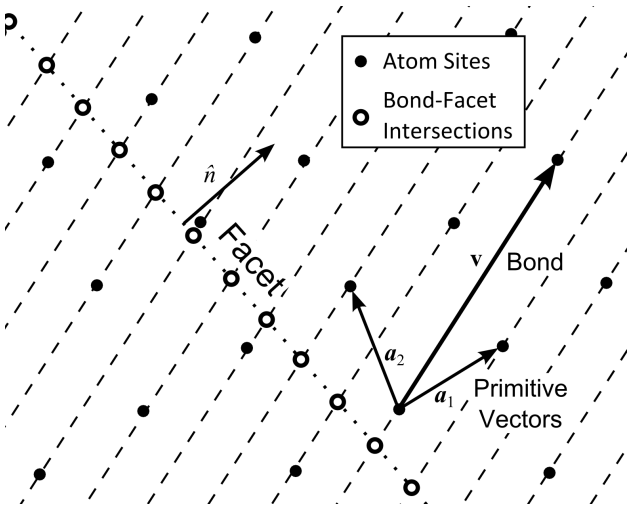


Figure 3.2: An illustration in two dimensions of a Bravais lattice, its two primitive vectors, a single bond corresponding to $\mathbf{v}$, a facet with normal $\hat{\mathbf{n}}$, and the collection of bond-facet intersections. The latter forms Bravais lattice in one fewer dimensions along the facet.

First, we show that on a 3D Bravais lattice, the intersections of bonds corresponding to a vector $\mathbf{v}$ with a planar facet form a 2D Bravais lattice on the facet. Choose vectors $\tilde{\mathbf{a}}_1, \tilde{\mathbf{a}}_2$ such that the set $\{\mathbf{v}, \tilde{\mathbf{a}}_1, \tilde{\mathbf{a}}_2\}$ spans the crystal lattice. Each of the bonds corresponding to $\mathbf{v}$ lies on a line of the form $\{t\mathbf{v} + k_1\tilde{\mathbf{a}}_1 + k_2\tilde{\mathbf{a}}_2 + k\mathbf{v} \,|\, k, k_i \in \mathbb{Z}, t \in \mathbb{R}\}$ as shown in Fig. 3.2. To find the intersections of these lines and the facet given by $\{\mathbf{x} \,|\, \hat{\mathbf{n}} \cdot (\mathbf{x} - \mathbf{x}_0) = 0\}$ we solve the equation

$$\hat{\mathbf{n}} \cdot (t\mathbf{v} + \sum_{i=1}^{2} k_i\tilde{\mathbf{a}}_i + k\mathbf{v} - \mathbf{x}_0) = 0.$$

Solving for t gives

$$t = \frac{\hat{\mathbf{n}} \cdot \mathbf{x}_0}{\hat{\mathbf{n}} \cdot \mathbf{v}} + k - \sum_{i=1}^{2} k_i \frac{(\hat{\mathbf{n}} \cdot \tilde{\mathbf{a}}_i)}{\hat{\mathbf{n}} \cdot \mathbf{v}}.$$

Then the set of intersections can be written

$$\left\{ \sum_{i=1}^{2} k_i \frac{(\hat{\mathbf{n}} \cdot \mathbf{v})\tilde{\mathbf{a}}_i - (\hat{\mathbf{n}} \cdot \tilde{\mathbf{a}}_i)\mathbf{v}}{\hat{\mathbf{n}} \cdot \mathbf{v}} + \frac{\hat{\mathbf{n}} \cdot \mathbf{x}_0}{\hat{\mathbf{n}} \cdot \mathbf{v}} \mathbf{v} \quad \middle| \quad k_i \in \mathbb{Z} \right\}.$$

Therefore, the set of intersections is generated by integer combinations of the two vectors $\left\{ \frac{(\hat{\mathbf{n}} \cdot \mathbf{v})\tilde{\mathbf{a}}_i - (\hat{\mathbf{n}} \cdot \tilde{\mathbf{a}}_i)\mathbf{v}}{\hat{\mathbf{n}} \cdot \mathbf{v}} \right\}$ and is then a 2D Bravais lattice.

Now, consider a bond-counting model on a Bravais lattice with bonds corresponding to a vector $\mathbf{v}$. In the case $z = 1$, i.e. bonds do not overlap. From above, we know that the bond intersections on the facet form a Bravais lattice so the area on the facet per intersection equals the area of a Voronoi cell of this lattice. Construct a prism centered on each $\mathbf{v}$ bond with the 2D Voronoi cell as its base and spanning the length of the bond. This is illustrated in a 2D analog for easier viewing in Fig. 3.3. These prisms tile $\mathbb{R}^3$ and correspond to exactly one atom of the 3D lattice and are therefore primitive cells and have volume $V = |\det A|$. The height of each cell in the direction of $\hat{\mathbf{n}}$ is $h = \text{proj}_{\hat{\mathbf{n}}} \mathbf{v} = |\hat{\mathbf{n}} \cdot \mathbf{v}|$. Therefore, the area per bond intersection on the facet is given by $h^{-1}V = \frac{|\det A|}{|\hat{\mathbf{n}} \cdot \mathbf{v}|}$.

When bonds do overlap, $z = \gcd(v_1, v_2, v_3) > 1$. Following the construction above yields prisms that overlap with density z. By dividing these cells into z disjoint prisms each with height $h = z^{-1}|\hat{\mathbf{n}} \cdot \mathbf{v}|$, we arrive at a cell that tiles $\mathbb{R}^3$ without overlapping and contains one node of the lattice. This cell is then a primitive cell with volume $V = |\det A|$, which determines the area of a Voronoi cell on the facet: $h^{-1}V = \frac{z \det A}{|\hat{\mathbf{n}} \cdot \mathbf{v}|}$. Then, since there are z bonds cut at each intersection, the number of bonds cut per unit area on a facet with normal $\hat{\mathbf{n}}$ is $z\frac{|\hat{\mathbf{n}} \cdot \mathbf{v}|}{z|\det A|} = \frac{|\hat{\mathbf{n}} \cdot \mathbf{v}|}{|\det A|}$.

Therefore, for $z \geq 1$, the bonds cut per unit area by a planar facet with normal $\hat{\mathbf{n}}$ is given by

$$\gamma_b(\hat{\mathbf{n}}) = \frac{|\hat{\mathbf{n}} \cdot \mathbf{v}|}{|\det A|} \tag{3.6}$$

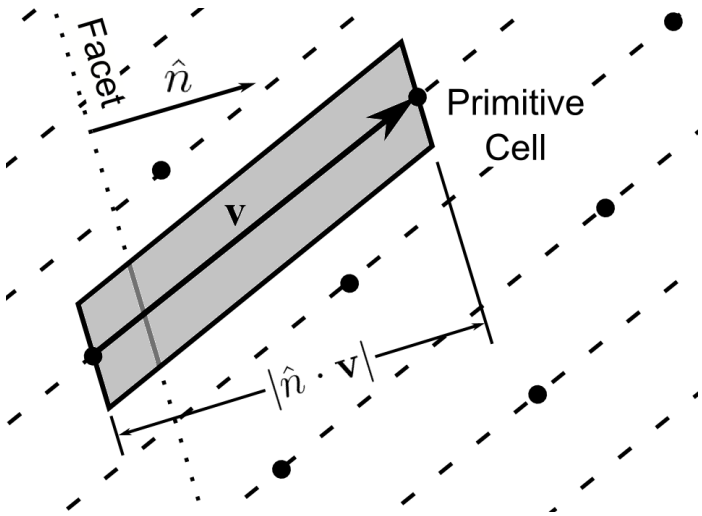


Figure 3.3: A 2D illustration of an arbitrary bond and a prismatic primitive cell with base parallel to a facet with normal $\hat{\mathbf{n}}$. In this case the Voronoi cell of facet intersections consists of a line segment and is shaded in the figure.

where $A = [\mathbf{a_1}, \mathbf{a_2}, \mathbf{a_3}]$ and z is the bond density.

In a model with multiple types of bonds, we can superimpose the contribution of each bond $\mathbf{v}_j$ using the corresponding weight w_j. Then the total surface energy for a facet with normal $\hat{\mathbf{n}}$ is

$$\gamma_b(\hat{n}) = \frac{\sum_{j=1}^{n_b} w_j |\hat{n} \cdot \mathbf{v}_j|}{|\det A|}. \tag{3.7}$$

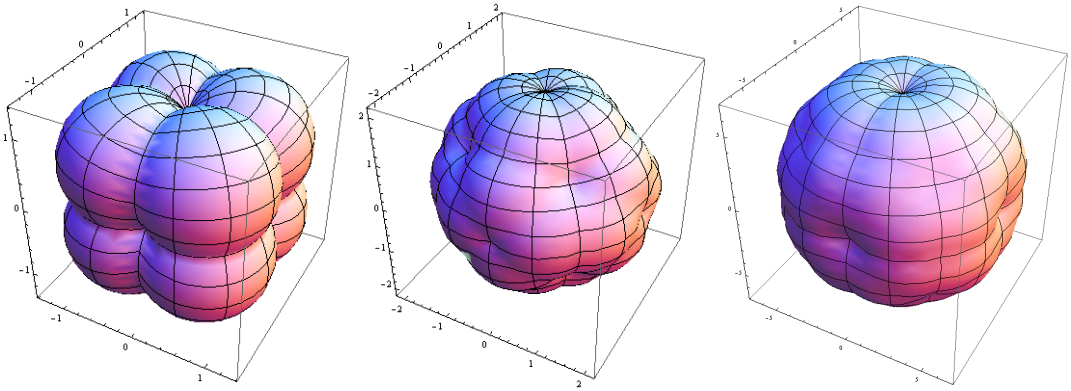
In the FCC examples that follow, the nearest-neighbor bonds share the weight w_1 and the next-nearest-neighbor bonds share the weight w_2. Surface energies for these examples take the form

$$\gamma_b(\hat{n}) = \frac{1}{|\det A|} \left(w_1 \sum_{i=1}^{6} |\hat{n} \cdot \mathbf{v}_{1i}| + w_2 \sum_{i=1}^{3} |\hat{n} \cdot \mathbf{v}_{2i}| \right), \tag{3.8}$$

where $\{\mathbf{v}_{1i}\}$ represent the bonds between FCC nearest-neighbors and $\{\mathbf{v}_{2i}\}$ the bonds between FCC next-nearest neighbors.

Fig. 3.4 contains examples of three-dimensional surface energies. Fig. 3.4a is the surface energy for a model counting nearest-neighbor bonds on a cubic lattice, each with weight $w = 1$. Fig. 3.4b counts nearest-neighbor bonds on a FCC lattice with

weights $w_1 = 1, w_2 = 0$. Fig. 3.4b counts nearest- and next-nearest-neighbor on a FCC lattice with equal weights $w_1 = 1, w_2 = 1$.



(a) $\gamma_b(\hat{n})$ for nearest-neighbor bonds on a cubic lattice

(b) $\gamma_b(\hat{n})$ for nearest-neighbor bonds on a FCC lattice

(c) $\gamma_b(\hat{n})$ for nearest- and next-nearest-neighbor bonds on a FCC lattice

Figure 3.4: Examples of Surface Energies

3.4 Equilibrium and Growth Shape

A crystal in equilibrium is not subject to conditions that will drive its growth. The equilibrium shape minimizes the total surface energy among competitors with fixed volume:

$$\min_{|\Omega|=V} \int_{\mathbf{x}\in\partial\Omega} \gamma(\hat{n}(\mathbf{x}))dS. \tag{3.9}$$

The minimizer is also known as the Wulff shape and is given by the well-known formula (Fonseca, 1991):

$$W = \{\mathbf{x} \in \mathbb{R}^3 | \mathbf{x} \cdot \hat{\mathbf{n}} \leq \gamma(\hat{\mathbf{n}}) \; \forall \hat{\mathbf{n}}\}. \tag{3.10}$$

The surface of the Wulff shape can be described with the function

$$w(\hat{\mathbf{d}}) = \min_{\hat{\mathbf{d}}\cdot\hat{\mathbf{n}}>0} \left[\frac{\gamma(\hat{\mathbf{n}})}{\hat{\mathbf{d}} \cdot \hat{\mathbf{n}}}\right] \tag{3.11}$$

where $\left\{\hat{\mathbf{d}}\right\}$ is the set of all unit vectors. This shape is constructed by drawing planes which are orthogonal to the radius vector at each point on the spherical plot of $\gamma(\hat{\mathbf{n}})$ and taking the inner envelope of those planes. A 2-dimensional example is illustrated in Fig. 3.5.

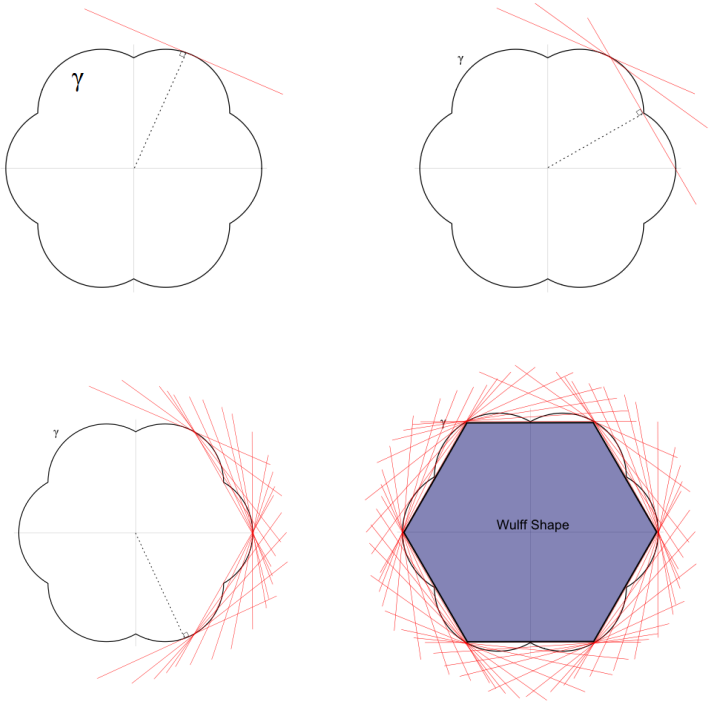
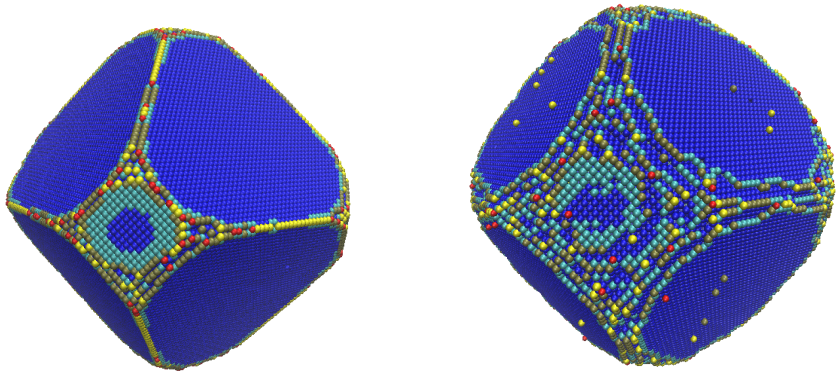


Figure 3.5: A 2-dimensional example of the Wulff construction using the edge energy function of nearest-neighbor bonds on the regular triangular lattice.

As noted previously, the surface energy γ_b that we have derived for our bond-counting model is the zero-temperature surface energy. One result of this is that surface energies of the form (3.7) have several cusps. These cusps are local minima of the surface energies and lead to the faceted Wulff shapes seen in Fig. 3.7a & b. At nonzero temperatures, these cusps and the corresponding sharp edges in the equilibrium shapes become rounded. While we cannot directly compute this entropic contribution to the surface energy, we can simulate its effect on the equilibrium shape, as illustrated in Fig. 3.6. Note that the qualitative shape of the crystal can be determined from the calculation of the Wulff shape for γ_b. Calculating the Wulff

shape is a useful tool for exploring the range of morphologies attainable within a given bond-counting model, as such calculations can be done with little effort compared to the lengthy simulations needed to generate the shapes shown in Fig. 3.6.

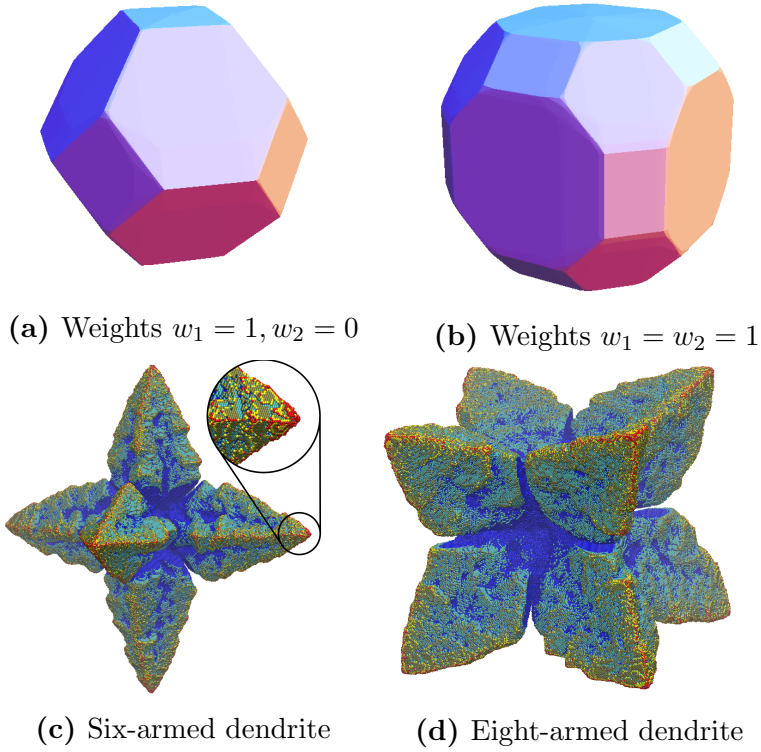


(a) Equilibrium Shape for $T = 351.7$ K

(b) Equilibrium Shape for $T = 580.2$ K

Figure 3.6: KMC simulations of an FCC crystal's equilibrium shape under two different temperatures, with energy scaled such that $w_1 = 0.1$ eV. Higher temperatures lead to softer edges as seen in b.

When a growing crystal is sufficiently small, surface diffusion will dominate the diffusive effects driving growth, so that the crystal evolves toward its equilibrium shape. The subsequent growth shape is more difficult to predict, but is heavily influenced by the equilibrium shape in that the crystal tends to grow more quickly in regions that are closest to the driving force in the far-field. In many cases, these fast growth directions, which are often easily predicted by inspection, continue to dominate the shape of the crystal. This effect is illustrated for six-armed dendrite in Fig. 3.7. The dendrite in Fig. 3.7c has six arms corresponding to square $\langle 100 \rangle$ facets of Fig. 3.7a, which are the furthest facets from the center of the Wulff shape. In Fig. 3.7d the eight arms correspond to the hexagonal $\langle 111 \rangle$ facets seen in Fig. 3.7b, but here we start to see that there are more complex mechanisms at play since the rectangular $\langle 110 \rangle$ facets are further away from the center and do not correspond to growth directions.



(a) Weights $w_1 = 1, w_2 = 0$ **(b)** Weights $w_1 = w_2 = 1$

(c) Six-armed dendrite **(d)** Eight-armed dendrite

Figure 3.7: FCC Wulff shapes and the corresponding results of a KMC simulation on a FCC lattice. The Wulff shapes in a & b correspond to the surface energies in Fig. 3.4b and c, which are both on a FCC lattice. The dendrite shown in c & d use the same parameters as the Wulff shapes in a & b respectively. These crystals each contain approximately 5×10^6 atoms, with the inset showing an atomic resolution close-up.

3.5 Discussion and Conclusion

The aim here is to explore the role of anisotropic surface energy in our KMC model, denoted γ_b, guided by what is known about the influence of surface energy in the context of continuum models, which we now will denote γ_c. Due to significant differences between the two models and the physical scenarios they represent, no direct comparison is intended here. Rather, our focus is on the class of morphologies that can be exhibited within each model at a given level of approximation.

We start by reiterating the differences between the two models. For the most part, the dendritic growth of a pure material into its own melt is modeled using the heat

equation along with appropriate boundary conditions. With some approximation, this can also be viewed as a model where the growth is occurring from a supersaturated vapor, a scenario that is more directly analogous to the KMC simulations described in the previous section. There is an extensive literature that examines the effects of both solute and heat diffusion on such processes (Davis, 2001). More significantly, we have already commented on the important distinction that γ_b is a zero-temperature surface energy, while γ_c represents the free energy at the melting temperature. Another important distinction between the KMC simulations and simulations based on the continuum model, is that the former are necessarily restricted to atomistic length scales due to computational requirements, whereas the latter are largely aimed at the macroscale. While most studies of dendritic growth are done on scales larger than can be simulated with KMC, there are experimental results that exhibit nanodendrites with highly developed branches with length scales similar to our simulations (W. Wang, 2013; Gh. Jiang, 2005).

Despite these differences, it is natural to wonder whether or not similar growth shapes can be exhibited in both models and, if not, why? Of particular interest is the possibility of 12-armed and 24-armed dendrites. While I was able to find evidence for the latter,I was not able to exhibit 12-armed dendrites using a nearest- and next-nearest-neighbor bond-counting model, i.e. longer range or multi-body interactions would appear to be necessary.

Recall that T. Haxhimali and Rappaz (2006) examined the effects of anisotropy in the solid-liquid interfacial free-energy for a class of functions given by a truncated expansion in terms of cubic harmonics:

$$\gamma_c(\theta, \phi) = \gamma_0[1 + \epsilon_1 K_1(\theta, \phi) + \epsilon_2 K_2(\theta, \phi)], \tag{3.12}$$

where the first three normalized cubic harmonic functions are (J.J. Hoyt and Karma, 2003):

$$\begin{aligned} K_0(\hat{n}) &= 1, \\ K_1(\hat{n}) &= \tfrac{\sqrt{21}}{4}[5(n_1^4 + n_2^4 + n_3^4) - 3], \\ K_2(\hat{n}) &= \sqrt{\tfrac{13}{128}}[21(n_1^4 + n_2^4 + n_3^4) + 462(n_1 n_2 n_3)^2 - 17]. \end{aligned}$$

One of the more intriguing shapes uncovered in these simulations, was a twelve armed dendrite that occurred when the K_1 contribution was absent, specifically for $\gamma_c(\hat{n}) = 1 - 0.02K_2(\hat{\mathbf{n}})$.

In an attempt to grow a crystal with a similar morphology using a KMC model, we first sought parameters that would give a similar functional form for γ_b. Like the spherical harmonics, cubic harmonics are orthonormal with respect to the inner product $\langle f, g\rangle = \frac{1}{4\pi}\int_{\partial B(0,1)} f \cdot g \, \mathrm{d}S$. This means any γ-plot, including γ_b of a bond-counting model, can be projected onto the cubic harmonics by:

$$\gamma_b(\hat{\mathbf{n}}) = \gamma_0(1 + \epsilon_1 K_1(\hat{n}) + \epsilon_2 K_2(\hat{n}) + \cdots), \tag{3.13}$$

where $\gamma_0 = \langle \gamma, 1\rangle$ is the average value of γ_b and $\epsilon_i = \frac{1}{\gamma_0}\langle \gamma, K_i\rangle$. Thus, we computed ϵ_1 and ϵ_2 for energies of the form (3.7) as a function of the nearest-neighbor bond strength (with the weight for nearest-neighbor bonds fixed at 1). The bond strength $w_2 = 0.353553$ gives $\epsilon_1 = 0$ and $\epsilon_2 = -0.0219097$, and therefore seems to be a good candidate for growing a twelve-armed dendrite.

Next, we consider a KMC simulation using this value of w_2. The result shown in Fig. 3.8 is a dendrite containing approximately 5×10^6 atoms. Rather than a 12-armed dendrite, there are 24 primary branches that eventually merge in groups of four to form six larger branches. While Haxhimali et al. did exhibit some 24-branched structures, these were computed using non-zero values of ϵ_1, and the 12-armed structure in their model seemed to correlate with small values of ϵ_1.

To understand why this might be the case, in Fig. 3.9, we examine the Wulff shapes corresponding to the surface energy functions for both models. The first (a)

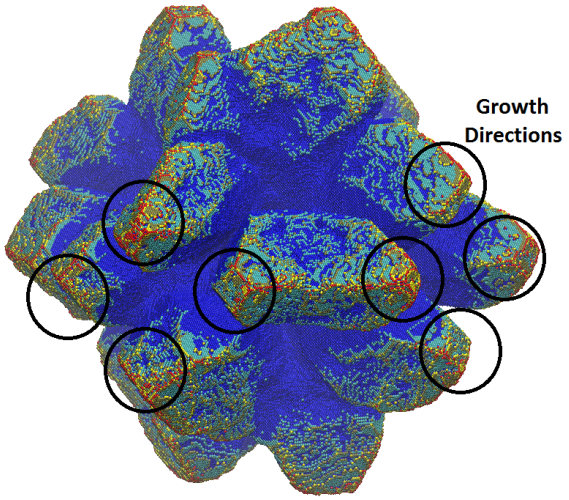
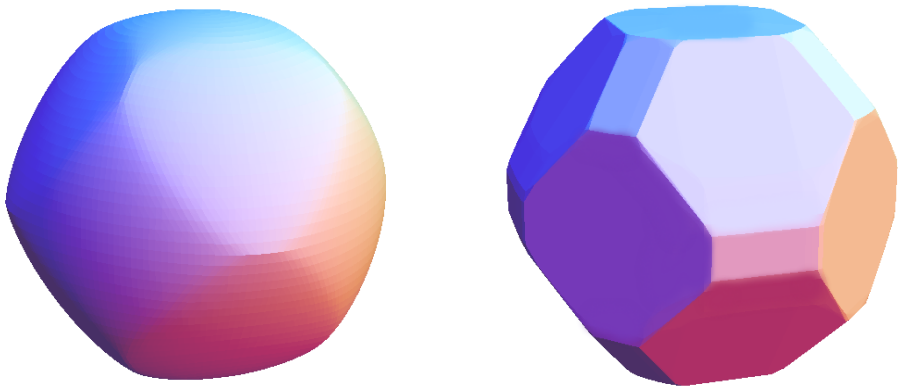


Figure 3.8: Kinetic Monte-Carlo simulation using the value $w_2 = 0.353553$, which has been chosen to eliminate ϵ_1 in the cubic harmonic expansion of the surface energy (3.13). This dendrite contains approximately 5 million atoms. Note that there are 24 primary branches (six groups of four) that seem to be merging into six larger branches.

corresponds to $\gamma_c(\hat{n}) = 1 - 0.2K_2(\hat{n})$, where $\epsilon_1 = 0$ and all harmonics beyond ϵ_2 are also zero. This surface energy matches that used by T. Haxhimali and Rappaz (2006) for the 12-armed dendrite shown in their Fig. 2(e). The second (b) corresponds to $\gamma_b(\hat{n}) = 1 - 0.2K_2(\hat{n}) + \cdots$, which is a surface energy for a bond-counting model with $\epsilon_1 = 0$ as a result of the choice $w_2 = 0.353553$. Note that the higher order harmonics are not necessarily zero, which accounts for the significant qualitative change in shape. In case (a) there are twelve cusps while case (b) is faceted with twelve smaller facets corresponding to the cusps in (a).

First we note that, since the first two cubic harmonic terms match in the two energies, the difference must be in the higher-order terms. Since the continuum model truncates after the second term, all higher-order coefficients are 0. In the expansion of γ_b, however, we can compute these coefficients directly:

$$\epsilon_3 = \int \gamma_b(\hat{\mathbf{n}}) K_3(\hat{\mathbf{n}}) = -0.0150347$$



(a) **(b)**

Figure 3.9: Wulff shapes corresponding to two surface energy functions. The first (a) corresponds to $\gamma_c(\hat{n}) = 1 - 0.02K_2(\hat{n})$. The second (b) corresponds to the FCC bond-counting model with $w_1 = 1$, $w_2 = 0.353553$ and has the cubic harmonic expansion $\gamma_b(\hat{n}) = 1 - 0.02K_2(\hat{n}) + \cdots$.

$$\epsilon_4 = \int \gamma_b(\hat{\mathbf{n}}) K_4(\hat{\mathbf{n}}) = 0.00150363$$

$$\epsilon_5 = \int \gamma_b(\hat{\mathbf{n}}) K_5(\hat{\mathbf{n}}) = -0.00665085$$

While these coefficients demonstrate the difference in the two energies, they are not very helpful in explaining exactly why the behaviors differ. Using numerical methods to determine the net flux of atoms onto the surface of the Wulff shape in Fig. 3.9b on an FCC lattice illustrates that there are two distinct high-flux regions on each of the shape's twelve small, rectangular $\langle 110 \rangle$ facets which seems to explain the 24-armed growth behavior. Similar analysis on the Wulff shape in Fig. 3.9a suggests that there is only one high flux region for each of its twelve $\langle 110 \rangle$ cusps, although the shape is too singular to get clear results on the lattice at the same resolution. Therefore, even though this bond-counting surface energy approximates the surface energy in Haxhimali et al., it appears that the difference between the corresponding surface energies is still too great to achieve the same behavior.

I have also considered how many terms the expansion of γ_c would need in order to see a Wulff shape for a continuum model similar to that of bond-counting models.

Using the computed coefficients of the cubic harmonic expansion of γ_b above, we computed the Wulff shapes for energies of the form $\sum_{i=1}^{n} \epsilon_i K_i(\hat{\mathbf{n}})$ for $n > 2$. It is interesting that just by adding the third term in the expansion, the Wulff shape is significantly more faceted, as seen in Fig. 3.10. However, it is only when the expansion includes the first five terms that the Wulff shape becomes fully faceted and a very good approximation of γ_b.



Figure 3.10: Wulff shape corresponding to surface energy $\gamma(\hat{\mathbf{n}}) = 1 - 0.02K_2 - 0.0150347K_3$.

Ultimately, we conclude that, at any finite level of approximation, both models exhibit a type of truncation error that makes them incompatible. In the continuum models, surface energy is modeled by truncating after one or more cubic harmonic terms. In bond-counting models, surface energy is the result of interactions between nearest-neighbors lying within some cutoff radius. It appears that a surface energy function within one of these families may lead to growth behavior not exhibited by functions in the other family using their respective models.

Chapter 4

Graphene Edge Energy

Analagous to the surface energy of 3D crystals of the previous section, a 2D crystal's bond-counting edge energy is calculated by counting the number of bonds intersected along an edge with normal $\hat{n}$. Edge energy for different edge orientations of a graphene lattice have been studied in multiple works since the discovery of graphene sheets at room temperature in 2009 (C. K. Gan, 2009; Y. Liu, 2010; P. Branicio, 2011). These papers all identify what is referred to as the 'zigzag' orientation as the edge orientation with minimum energy for non-stressed graphene sheet. This is consistent with experimental results that show that it is the preferred orientation for graphene nano ribbons. However, the minimum value of edge energy may not be the only energy value of a graphene edge with the same orientation.

The fact that some graphene edges have variable edge energy is illustrated in Fig. 4.1. For some edges, edge energy when counting nearest-neighbor bonds is invariant under translation but for others, edge energy does change on translation of the edge. In this example, there are only two discrete values of the energy and we will see that this is true for all graphene edges with multi-valued edge energy.

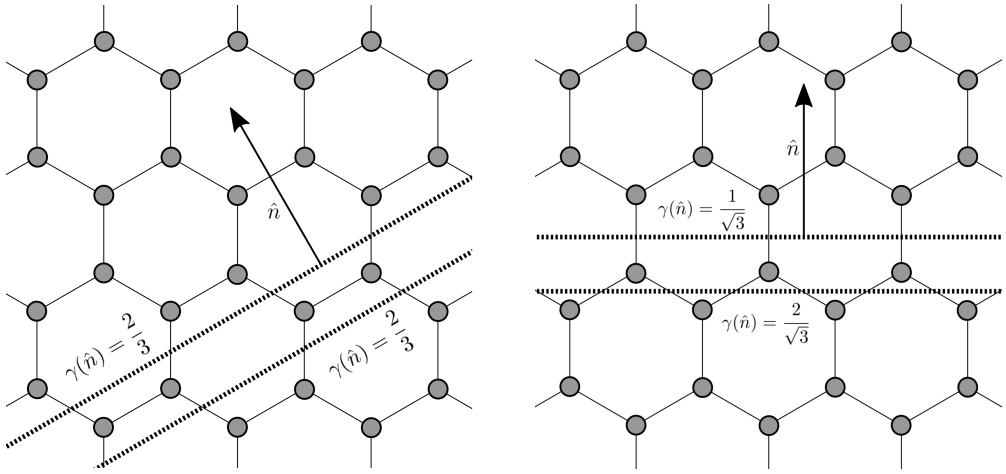


Figure 4.1: In (a), we see two edges with the same normal $\hat{n} = (-1/2, \sqrt{3}/2)$ that also share the edge energy $\gamma(\hat{n}) = 2/3$. Any edge with this same normal will also have that same edge energy. However, in (b), two edges are shown with normal $\hat{n} = (1, 0)$ and yet have different energies. These are the only two edge energy values exhibited by edges with this normal.

Recall the formula for the calculation of surface energy for models on a Bravais lattice, which works for 2D Bravais lattices as well:

$$\gamma(\hat{\mathbf{n}}) = \sum_i w_i \frac{|\hat{\mathbf{n}} \cdot \mathbf{v}_i|}{|\det A|} \tag{4.1}$$

where $\hat{\mathbf{n}}$ is normal to the edge, $\{\mathbf{v}_i\}$ is the set of bonds considered, and A is the matrix with lattice primitive vectors as columns.

Bond-counting models on a Bravais lattice have the useful property that any two edges with the same orientation have the same edge energy. However, crystals on a non-Bravais lattice do not share this property and graphene is not a Bravais lattice. We seek the tools to be able to calculate the edge energy not only for the nearest-neighbor bond-counting model of graphene, but for more generalized models counting more bonds and/or occuring on different non-Bravais lattices in 2 or 3 dimensions.

While the graphene lattice is not a Bravais lattice, it is what is referred to as a lattice with a basis. The basis consists of two atoms, one of type A and one of

type B which can then be used to tile the plane in a Bravais lattice. Atoms of type A have one set of nearest-neighbor directions while atoms of type B have another. For the purposes of this work, let atoms with nearest-neighbors in the directions $\{(0,1),(\pm\sqrt{3}/2,-1/2)\}$ be of type A and let atoms with nearest-neighbor directions $\{(0,-1),(\pm\sqrt{3}/2,1/2)\}$ be type B.

In order to fully characterize edge energy on a non-Bravais lattice, we divide the set of all edge orientations into three cases:

1. Commensurate edge orientations for which edge energy is invariant under translation. We will refer to these as "uniform" orientations.

2. Commensurate edge orientations for which edge energy is multi-valued under translation, hereafter referred to as "funny" orientations.

3. Orientations such that if the edge passes through one atom, it doesn't pass through another, or "noncommensurate" directions.

Before we proceed, it's important to note how this work relates to other studies on the edge energy of graphene. For the most part, other works measure the energy for a small set of discrete orientations related to the symmetries of the lattice, using either physical experimentation or high-powered computing methods like density functional theory. Afterwards, various interpolation methods are used to estimate the whole curve. While the bond-counting model used in this work is more simplistic, we can essentially compute the entire picture and discover some interesting effects lost in the process of only using a small set of orientations.

4.1 Edge Energy Calculation

In this section, we derive the edge energy for graphene only counting nearest neighbor bonds. As with Bravais lattice models, we can compute energy values for a particular bond orientation and sum over the whole bond set to derive the total surface energy.

Now each type of graphene atom has a different set of bonds, but for each bond $\mathbf{v}$ in one set, $-\mathbf{v}$ is a bond in the other. Therefore, we only need to use one of the two sets of bonds to count all bonds cut per unit length along an edge.

Pick a bond orientation vector $\mathbf{v}$ and rotate the lattice such that $\mathbf{v}\cdot(1,0)=0$. We start by defining the sequence $\alpha=\{\alpha_1,\alpha_2,\dots\}$ where α_n takes values in the interval $[0,3]$ corresponding to where the edge intersects each bond-line period. A bond is cut at the nth bond-line if $\alpha_n\in(0,1)$ as shown in Fig. 4.2.

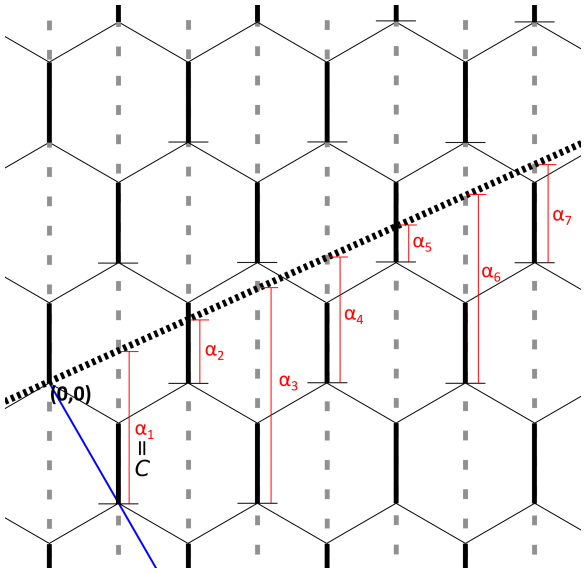


Figure 4.2: An example of an edge and its sequence α.

With the lattice oriented this way, we can directly calculate each α_n. Let the slope of the edge be given by s and without loss of generality, let the origin be at a node of the lattice. For all $n\in\mathbb{N}$, α_n is the remainder when dividing nC by 3, where $C=\left(s\frac{\sqrt{3}}{2}+\frac{3}{2}\right)$. C can be understood as the signed distance from the point $(\sqrt{3}/2,-3/2)$ to the edge's intersection with the first bond-line.

Note that an edge with slope s is commensurate if and only if $\sqrt{3}s\in\mathbb{Q}$. This is readily apparent since $\sqrt{3}s\in\mathbb{Q}$ implies $C\in\mathbb{Q}$ and $nC\in\mathbb{Z}$ for some n. And when $nC\in\mathbb{Z}$ the bond-line intersection corresponding to α_n occurs at a node of the refined Bravais lattice, making the edge commensurate.

Another important observation is that an α sequence for a commensurate edge repeats values over a finite period. This is a consequence of the existence of the refined Bravais lattice. Any commensurate edge on a Bravais lattice that can be drawn through one node passes through an infinite number of atoms and each atom is indistinguishable from another. On the graphene lattice, not only must a commensurate edge pass through an infinite number of atoms, it passes through an infinite number of atoms of the same type as the first. If we let the origin atom be of Type A, we can translate the entire lattice so that some other Type A atom lying on the edge is mapped to the origin and the result of recalculating α would be identical to the original. Thus α is repeating and let $b_{\mathbf{v}} \in \mathbb{Z}$ be the period of α.

4.1.1 Bravais Refined Lattice

In the previous chapter, I have detailed the calculation of edge energies for an ideal crystal on any Bravais lattice. The graphene lattice has a nice relationship with the Bravais lattice generated by primitive vectors $(\sqrt{3}/2, 1/2)$ and $(0, 1)$, namely that you can construct the Bravais lattice by placing a node at the center of each hexagonal cell of the graphene lattice as shown in Fig. 4.3. As a result, these two lattices share a property that makes our job in trying to calculate the edge energy of the graphene lattice much easier: they share the same bond-lines. Any bond-line constructed on one coincides with a bond-line on the other. The set of bond-lines on each lattice is the same, but the difference in edge energy arises as a consequence of the gaps between bonds within bond-lines on the graphene lattice. The density of bonds along a bond-line on a Bravais lattice is always constant but on a non-Bravais lattice it need not be.

Consider three classes of nodes on this Bravais refined lattice: type A and B nodes which coincide with type A and B atoms respectively on the graphene lattice and a third type C which were placed as part of the Bravais lattice's construction at the centers of the hexagonal cells of graphene. If we were to extend a line in the direction

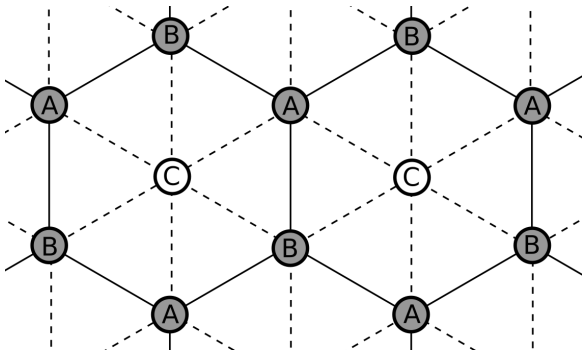


Figure 4.3: The construction of the graphene lattice's corresponding Bravais refined lattice.

of a funny edge through a node of the refined lattice, it would pass through an infinite number of nodes of the same type and not through any other nodes. Consider the collection of all such lines. Note that since these lines lie on a Bravais lattice, they are all equally spaced. Lines that pass through type A and B atoms are the borders of energy bands on the graphene lattice since each bond that has funny directions is shared by one type A atom and one type B atom. Thus, as a funny edge is translated through one of these lines it either loses or gains a bond and changes energy values.

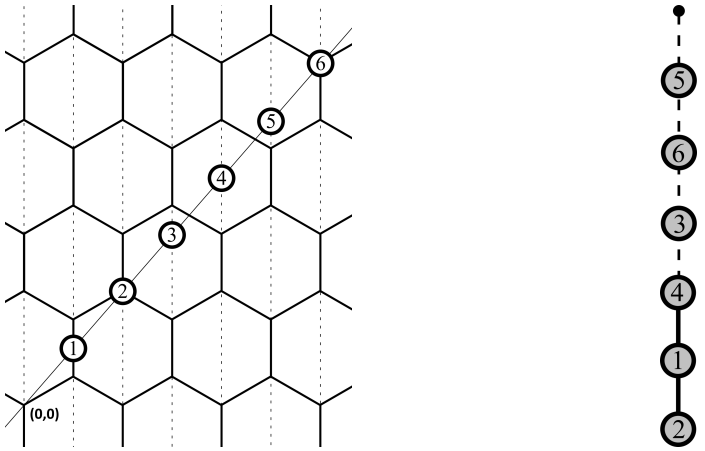
Let $\Gamma_{\mathbf{v}}(\hat{\mathbf{n}})$ be the number of $\mathbf{v}$ bonds cut by an edge on the Bravais refined lattice per unit length and let $\Gamma(\hat{\mathbf{n}}) = \sum_{\mathbf{v}\in V} \Gamma_{\mathbf{v}}(\hat{\mathbf{n}})$. I will compute the graphene energy for an edge with normal $\hat{\mathbf{n}}$ in terms of $\Gamma(\hat{\mathbf{n}})$.

4.1.2 Uniform Edges

Theorem 4.1. *An edge orientation of graphene is uniform with respect to nearest-neighbor bonds if and only if* $3 \mid b_{\mathbf{v}}$ *or equivalently, if when the edge passes through an atom of type A, it must also pass through an atom of type B.*

If $3|b_{\mathbf{v}}$ then $\alpha_n = 1$ and $\alpha_m = 2$ for some $m, n < b_{\mathbf{v}}$, corresponding to intersections at a type-A node and a type-B node respectively as shown in Fig. 4.4. This leads to a uniform edge because when translating such an edge across the lattice, whenever the edge ceases to cut a particular $\mathbf{v}$-bond by passing through a type A atom, it picks

up another **v**-bond by passing through a type B atom. Since a new bond is picked up every time a bond is lost, the number of bonds cut per unit length never varies.



(a) **(b)**

Figure 4.4: Here the bond intersections on one period of a uniform edge are illustrated.

Note that since the values of α within a period are evenly distributed in $[0, 3]$, for a uniform edge, one third of the α_n values in a period lie in the interval $(0, 1]$ and correspond to a bond crossing. Thus one third of bond-line intersections occur at bonds on the graphene implying that the edge energy is one third that of the same edge on the Bravais refined lattice. Therefore the edge energy for a uniform direction is given by

$$\gamma(\hat{\mathbf{n}}) = \frac{1}{3}\Gamma(\hat{\mathbf{n}}) = \frac{2}{3\sqrt{3}} \sum_{i=1}^{3} |\hat{\mathbf{n}} \cdot \mathbf{v}_i| \tag{4.2}$$

where $\mathbf{v}_1 = (\sqrt{3}/2, 1/2), \mathbf{v}_2 = (-\sqrt{3}/2, 1/2), \mathbf{v}_3 = (0, 1)$. For the armchair orientation (e.g. $\hat{\mathbf{n}} = (1, 0)$), this gives an edge energy value of $2/3$.

One thing to note here is that the edge energy $\frac{1}{3}\Gamma(\hat{\mathbf{n}})$ has a hexagonal Wulff shape with edges in the armchair orientation, since those are the minimal energy directions in Γ. However in simulations and experimental results alike, the equilibrium shape of graphene is a hexagon with zigzag edges, which is a funny orientation. In fact, in KMC simulations in which atoms are arranged in an armchair hexagon, the crystal still seeks zigzag orientation edges in equilibrium as shown in Figure 4.5.

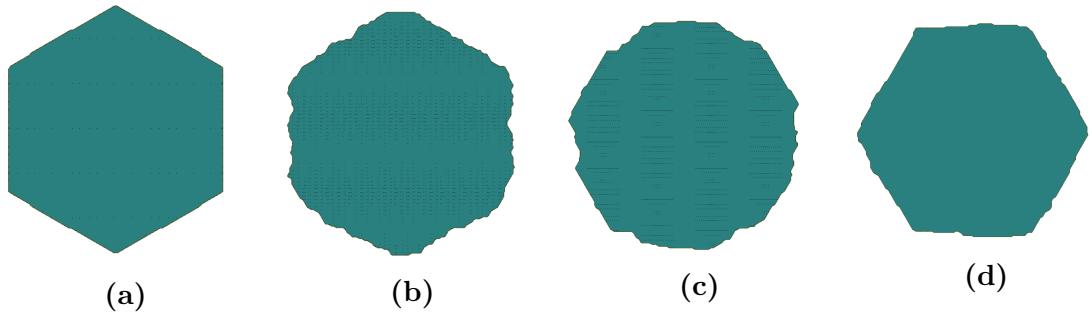


Figure 4.5: Results of equilibrium KMC simulation on a hexagonal lattice. In (a), atoms are initially arranged as a hexagon with armchair orientation edges. In (b), the crystal seeks zigzag edges very quickly and eventually achieves a hexagonal shape in (d) with fully zigzag orientation edges.

4.1.3 Funny Edges

Zigzag orientation edges can only pass through one type of atom, making it a funny direction. As shown above, there are two distinct edge energy values for zigzag edges. The minimum value is $1/\sqrt{3}$, which is lower than armchair energy, but the maximum value is $2/\sqrt{3}$. The fact that graphene seeks zigzag orientation edges at equilibrium suggests that the minimum edge energy value for a funny orientation drives growth behavior.

Now we calculate edge energy for all funny edges of graphene. Since they are commensurate, funny edges have a repeating sequence α but in the case of funny edges, $b_{\mathbf{v}} \equiv 1$ or $2 \mod 3$. Then there is no way to have exactly one third of the α_n values occur in $(0, 1]$ and, depending on the position of the edge, the energy will take a value above or below $\Gamma_{\mathbf{v}}$. For example, the funny edge in Fig. 4.6 has $b_{\mathbf{v}} = 5$ and in its current position two of the five distinct α_n take values in $(0, 1]$ but if the edge were translated a slight distance down, only one α_n would be in $(0, 1]$.

Define the edge's period length p to be the distance between atoms of the same type along the facet. If $b_{\mathbf{v}} \equiv 1 \mod 3$, the number of intersections on a bond per length p is $(n-1)/3$. Therefore the lesser of the two edge energies is given by

$$\gamma_{\mathbf{v}}^{-}(\hat{\mathbf{n}}) = \frac{n-1}{3p} = \frac{p\Gamma_{\mathbf{v}}(\hat{\mathbf{n}}) - 1}{3p} = \frac{1}{3}\Gamma_{\mathbf{v}}(\hat{\mathbf{n}}) - \frac{1}{3p}.$$

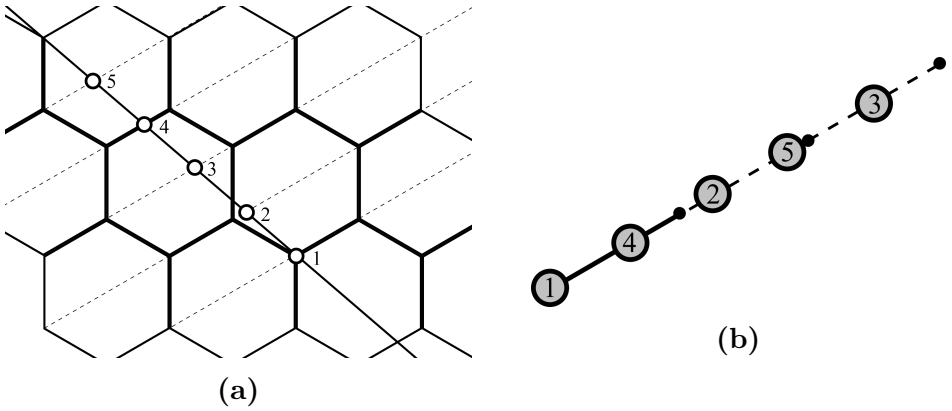


Figure 4.6: Here the bond intersections on one period of a funny edge is illustrated.

Similarly the greater edge energy which occurs for one third of the possible translations is

$$\gamma_{\mathbf{v}}^{+}(\hat{\mathbf{n}}) = \frac{1}{3}\Gamma_{\mathbf{v}}(\hat{\mathbf{n}}) + \frac{2}{3p}.$$

And if $b_{\mathbf{v}} \equiv 2 \mod 3$, the two edge energy values are

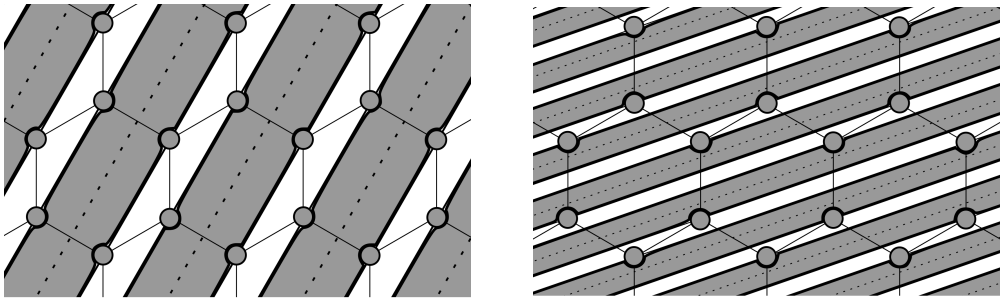
$$\gamma_{\mathbf{v}}^{-}(\hat{\mathbf{n}}) = \frac{1}{3}\Gamma_{\mathbf{v}}(\hat{\mathbf{n}}) - \frac{2}{3p},\ \gamma_{\mathbf{v}}^{+}(\hat{\mathbf{n}}) = \frac{1}{3}\Gamma_{\mathbf{v}}(\hat{\mathbf{n}}) + \frac{1}{3p}.$$

Since each funny direction has two distinct edge energy values, we can identify "bands" on the lattice in which each edge has the same energy value, as shown in Fig. 4.7. The edge energy within a single band is invariant under translation regardless of the choice of bonds. However, within a band, some bonds may contribute the maximum value $\gamma_{\mathbf{v}}^{+}$ while others contribute the minimum value $\gamma_{\mathbf{v}}^{-}$. In order to calculate the total edge energy within any band for any funny orientation, we present methods for determining whether a bond's energy takes $\gamma_{\mathbf{v}}^{+}$ or $\gamma_{\mathbf{v}}^{-}$ for a particular bond.

Proposition 1. *For any funny orientation, bands take on two different widths, one being twice as wide as the other.*

Proof. Consider the graphene lattice's corresponding Bravais lattice: the regular triangular lattice and the collection of lines that pass through each lattice node in

the direction of the facet as above. Lines that pass through type C atoms on the triangular lattice lie equally spaced between A and B lines, meaning that they lie in the middle of half of the bands. These bands are then twice as wide as the others. □



(a) **(b)**

Figure 4.7: Energy bands for two different funny edge orientations. The edges in (a) have normal $\hat{\mathbf{n}} = (-\sqrt{3}/2, 1/2)$ and the edges in (b) have normal $\hat{\mathbf{n}} = \left(-\frac{3}{2\sqrt{2}}, \frac{5}{2\sqrt{7}}\right)$.

Proposition 2. *The number of funny edge lines on the triangular lattice crossed by a single* $\mathbf{v}$ *bond is equal to* $b_{\mathbf{v}}$.

Proof. On the corresponding Bravais lattice, the number of bond intersections per unit length is $\gamma(\hat{\mathbf{n}})$. Then $b_{\mathbf{v}} = p\gamma(\hat{\mathbf{n}})$. And since this is a funny edge, it only intersects one atom on a length of p, meaning that each intersection on a bond corresponds to one intersection on a edge segment of length p. □

This is important because each of these bonds cross bands of the same width at each end of the band and it is within these bands that the edge energy takes the value $\gamma^+_{\mathbf{v}}$. If $b_{\mathbf{v}} \equiv 1 \mod 3$, the thin bands give the value $\gamma^+_{\mathbf{v}}$ and the wide bands give the value $\gamma^-_{\mathbf{v}}$. The opposite holds if $b_{\mathbf{v}} \equiv 2 \mod 3$.

Therefore we can determine the total edge energy for a funny edge within each of the two energy bands given any set of bonds $\mathbf{v}_i$. The edge energy for a edge within a thin band is given by

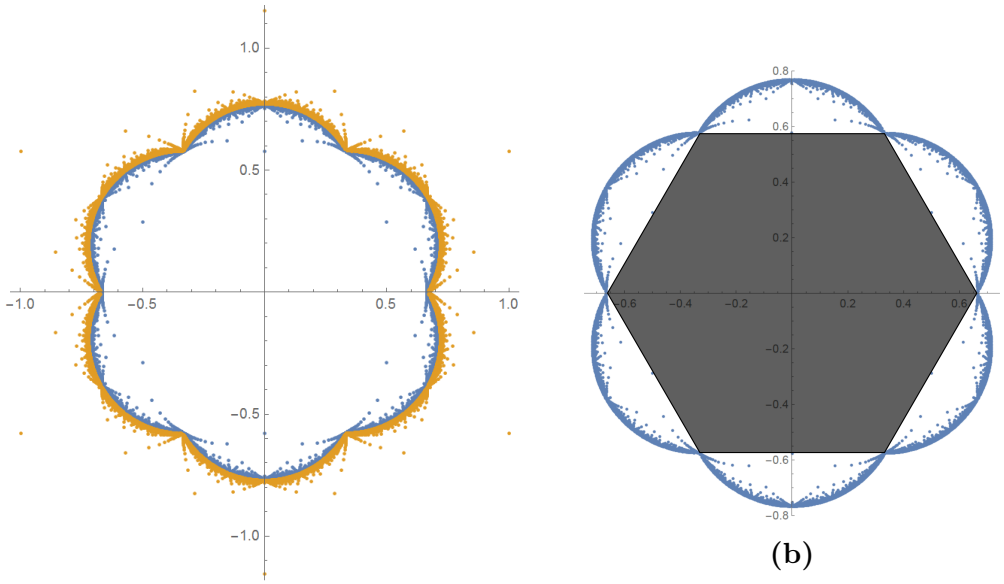
$$\gamma_1(\hat{\mathbf{n}}) = \sum_{b_{\mathbf{v}_i} \equiv 1 \bmod 3} \gamma^+_{\mathbf{v}_i}(\hat{\mathbf{n}}) + \sum_{b_{\mathbf{v}_i} \equiv 2 \bmod 3} \gamma^-_{\mathbf{v}_i}(\hat{\mathbf{n}}) = \frac{1}{3}\Gamma(\hat{\mathbf{n}}) + \frac{2}{3p}(m_1 - m_2) \tag{4.3}$$

where m_i is the number of bonds in $\{\mathbf{v}\}$ for which $b_{\mathbf{v}} \equiv i \bmod 3$. Similarly, the edge energy for a edge within a thick band is

$$\gamma_2(\hat{\mathbf{n}}) = \frac{1}{3}\Gamma(\hat{\mathbf{n}}) + \frac{1}{3p}(m_2 - m_1). \tag{4.4}$$

Note that $|\gamma_1 - \frac{1}{3}\Gamma| = \frac{2}{3p}|m_1 - m_2|$ and $|\gamma_2 - \frac{1}{3}\Gamma| = \frac{1}{3p}|m_1 - m_2|$ which means that $\lim_{p\to\infty} |\gamma_1 - \frac{1}{3}\Gamma| = \lim_{p\to\infty} |\gamma_2 - \frac{1}{3}\Gamma| = 0$.

Let $\gamma^-(\hat{\mathbf{n}}) = \min\{\gamma_1(\hat{\mathbf{n}}), \gamma_2(\hat{\mathbf{n}})\}$ and $\gamma^+(\hat{\mathbf{n}}) = \max\{\gamma_1(\hat{\mathbf{n}}), \gamma_2(\hat{\mathbf{n}})\}$. We can confirm that zigzag orientations minimize γ^- by calculating γ^- along all funny directions with p below some threshhold value, as shown in Fig. 4.8. For large p, both edge energies are close to Γ so as long as the minimum value of γ^- for low p is less than Γ for all $\hat{\mathbf{n}}$, it is the minimum edge energy value for all edges on the crystal. It is interesting that if we perform the classical Wulff construction using γ^- as the edge energy, we get a hexagon with zigzag orientation edges, coinciding with the graphene equilibrium shape, as shown in Fig. 4.8b.



(a) **(b)**

Figure 4.8: A graph of γ^- in blue and γ^+ in gold is shown in (a). In (b), we show the result of the Wulff construction using γ^-.

4.1.4 Non-Commensurate Edges

Edge energy along an edge with non-commensurate orientation is a different beast altogether. Commensurate edges are periodic in that they break the same number of bonds over some period all along the edge. A non-commensurate edge however, can only pass through one atom at once and does not have any sense of periodicity. The edge energy is meaningful only if defined as the mean number of bonds cut across the entire edge.

A natural hypothesis for this mean is the same value as uniform edge energies: $\frac{1}{3}\Gamma(\hat{n})$. This would be good news, as edge energies are simple to calculate on a Bravais lattice, even for non-commensurate directions. We demonstrate that this is in fact the edge energy for all non-commensurate directions.

Theorem 4.2. *The energy along a non-commensurate edge, defined as the mean number of bonds cut per unit length by the edge, is given by* $\gamma(\hat{n}) = \frac{1}{3}\Gamma(\hat{n})$.

Proof. For a non-commensurate edge, $\sqrt{3}s \in \mathbb{I}$, meaning that C is irrational; otherwise, Cn would take integer values for some n and the edge would pass through another atom and be commensurate. In this case, not only does α not repeat, but all of the infinite α_n values are distinct. Then, by Weyl's equidistribution theorem (Weyl, 1916), the set of all α_n is uniformly distributed in $[0, 3]$. This implies that one third of all α_n are in $(0, 1]$ and therefore, one third of all bond-line intersections occur at a bond.

The same result holds for each $\mathbf{v} \in \{\mathbf{v}_i\}$ and therefore

$$\gamma(\hat{n}) = \sum_i \frac{1}{3}\Gamma_{\hat{\mathbf{v}}_i}(\hat{n}) = \frac{1}{3}\Gamma(\hat{n}).$$

□

4.2 Generalization for All Graphene Bonds

Bonds between graphene atoms can be classified as follows:

1. Bonds between atoms of the same type.

2. Bonds between a type A atom and a type B atom

A bond corresponding to a vector $\mathbf{v}$ that occurs between atoms of the same type has the property that each atom shares two bonds with orientation $\mathbf{v}$. This means that each bond-line has a constant bond density which further implies that there are no funny directions with respect to such a bond.

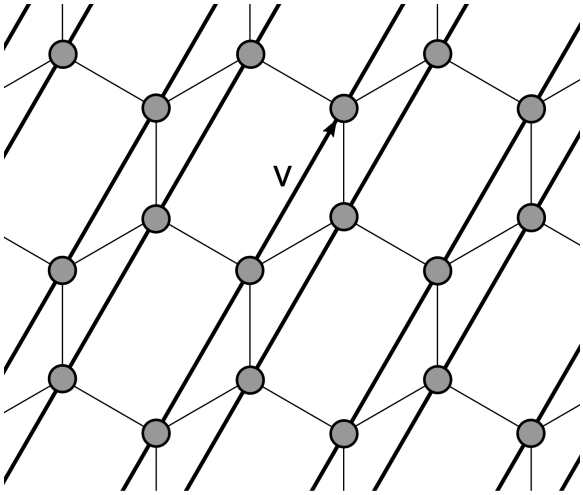


Figure 4.9: Next-nearest-neighbor bonds occur between atoms of the same type.

However, in the case of graphene these bond-lines are no longer equally spaced, as shown in Fig. 4.9. To see this, consider the Bravais refined lattice discussed earlier. If we plot the $\mathbf{v}$ bond-lines on the Bravais lattice, one third of the lines are formed by bonds between type C atoms and thus only intersect type C atoms. The graphene lattice doesn't contain any type C atoms and therefore has two-thirds the number of bond-lines and the edge energy for $\mathbf{v}$ bonds is given by

$$\gamma_{\mathbf{v}}(\hat{n}) = \frac{2}{3}\Gamma_{\mathbf{v}}(\hat{n})$$

for all edge orientations.

Bonds with a vector $\mathbf{v}$ between atoms of differing types are more complicated. Nearest-neighbor bonds are in this class and we've demonstrated that it's energy is given by

$$\gamma(\hat{\mathbf{n}}) = \frac{1}{3}(\Gamma_{\mathbf{v}}(\hat{\mathbf{n}}) \pm E)$$

where $E = 0$ for uniform edges. This formula holds for all $\mathbf{v}$ between type A and type B atoms including those shown in Fig. 4.10.

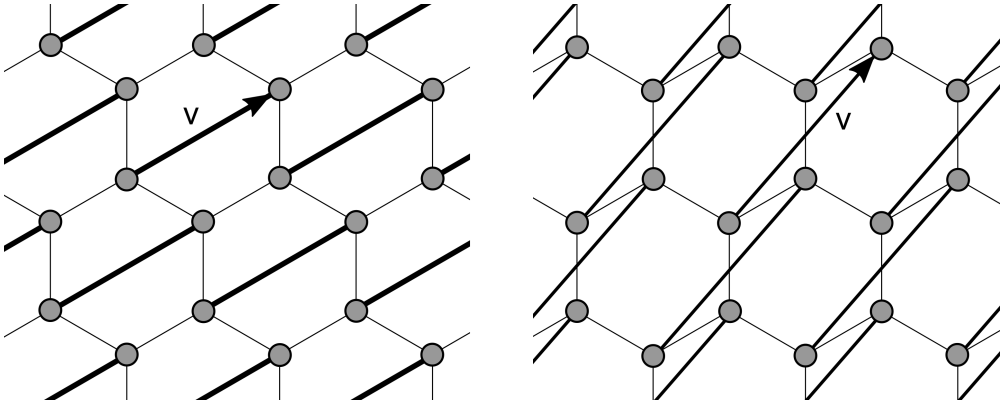


Figure 4.10: Next-next- and next-next-next-nearest neighbor bonds. Next-next-nearest-neighbor bonds shown in (a) do occur between A-type and B-type atoms, but they are in the same direction as nearest-neighbor bonds. Next-next-next-nearest-neighbor bonds with $\mathbf{v} = (\sqrt{3}, 2)$ are shown in (b).

The bond direction $\mathbf{v}$ illustrated in Fig. 4.10a is an interesting case. Note that $\mathbf{v} = 2(\sqrt{3}/2, 1/2)$ and that $\mathbf{v}' = (\sqrt{3}/2, 1/2)$ is a nearest-neighbor direction. Their bond-lines are obviously the same and thus have the same funny edges. The continuous part of γ is still given by $\gamma_{\mathbf{v}}(\hat{\mathbf{n}}) = \frac{1}{3}\Gamma_{\mathbf{v}}$, although note that $|\mathbf{v}| = 2|\mathbf{v}'|$ implies that $\Gamma_{\mathbf{v}} = 2\Gamma_{\mathbf{v}'}$. However, $\gamma_{\mathbf{v}}$ takes max and min values in bands opposite those of $\gamma_{\mathbf{v}'}$. These two bond directions might well be denoted complimentary bonds.

4.3 Comparison with Graphene Literature

C. K. Gan (2009) were the first to address the issue of edge energy for individual graphene flakes. They use DFT calculations for a collection of graphene ribbons at seven different orientations to interpolate an edge energy function. They consider unreconstructed graphene with both non-terminated and hydrogen terminated bonds, as well as a model for re-constructed graphene. They find that the unreconstructed graphene edge energy function has maxima at zigzag orientations, unlike the edge energy function calculated in this work. This inconsistency is due to the simplicity of the bond-counting model we've used and the much more accurate energy measurements of DFT. However, the existence of funny directions is a consequence of the lattice structure of graphene and not the energy potential used in the model. Interestingly, Gan and Srolovitz later demonstrate a shift in orientation as an unreconstructed graphene flake is allowed to relax and reconstruct, giving an equilibrium shape identical to those shown earlier in this chapter.

Y. Liu (2010) revisit the problem and first consider an arbitrarily oriented graphene edge that can be decomposed into a number of zigzag and armchair components, so that the edge energy can be represented using two energies of these primary configurations along with zigzag and armchair densities that can be computed from simple geometric considerations yielding a continuous energy function. Again, this function differs from those calculated here due to differences in the models. They include as parameters the terms ϵ_A and ϵ_Z defined as the edge energy contribution from each atom in an armchair or in a zigzag component respectively. The values they used for these terms are derived from DFT calculations which show $\epsilon_A < \epsilon_Z$. In bond-counting models, we assume that each bond contributes equally to edge energy and since both zigzag and armchair atoms are two-coordinated, $\epsilon_A = \epsilon_Z$ in a graphene bond-counting model.

The edge energy function used by Liu et al. is given by

$$\gamma_L(\hat{\mathbf{n}}) = (4/\sqrt{3})\epsilon_A \sin(\pi/6 - \theta_{\hat{\mathbf{n}}}) + 2\epsilon_Z \sin(\theta_{\hat{\mathbf{n}}})$$

for $\theta_{\hat{\mathbf{n}}} \in [-\pi/6, \pi/6]$ and the rest of the function is determined by symmetry. The result of overlaying γ_L onto the edge energy plot of this chapter, setting $\epsilon_A = \epsilon_Z$ and scaling so that $\gamma_L((1,0)) = \gamma((1,0))$, is shown in Fig. 4.11. Note that some of the γ_- values are coincide with γ_L values. These orientations correspond with all edges for which the minimum energy configuration does not have any singly-bonded atoms. In fact, in Liu et al.'s derivation of this function, the zigzag and armchair components do not contain any singly-bonded atoms. This implies that their edge energy function is for graphene edges after the removal of any such atoms, leading to a single-valued function. They do not seem to justify this choice. It may be due to the idea that any singly-bonded atom is too weakly connected to a graphene flake to stay in equilibrium. However, these atoms do occur in an atomistic growth model of graphene and funny directions should have an effect on growth behavior.

4.4 KMC Experimentation

We have established the existence of funny edge orientations for graphene and identified the effect thereof on graphene edge energy but what effect, if any, do funny edges have on the growth behavior of graphene. We have already seen the qualitative results of a KMC simulation for the equilibrium shape of a graphene flake in Fig. 4.5, but let us now compare similar simulations on both the graphene and the triangular lattice.

In Fig. 4.12 we see two KMC equilibrium shape simulations. The top row shows the time evolution of a flake with regular triangular lattice structure with $w/(k_bT) = 10$ and the bottom row depicts a simulation of a graphene flake with $w/(k_bT) = 15$.

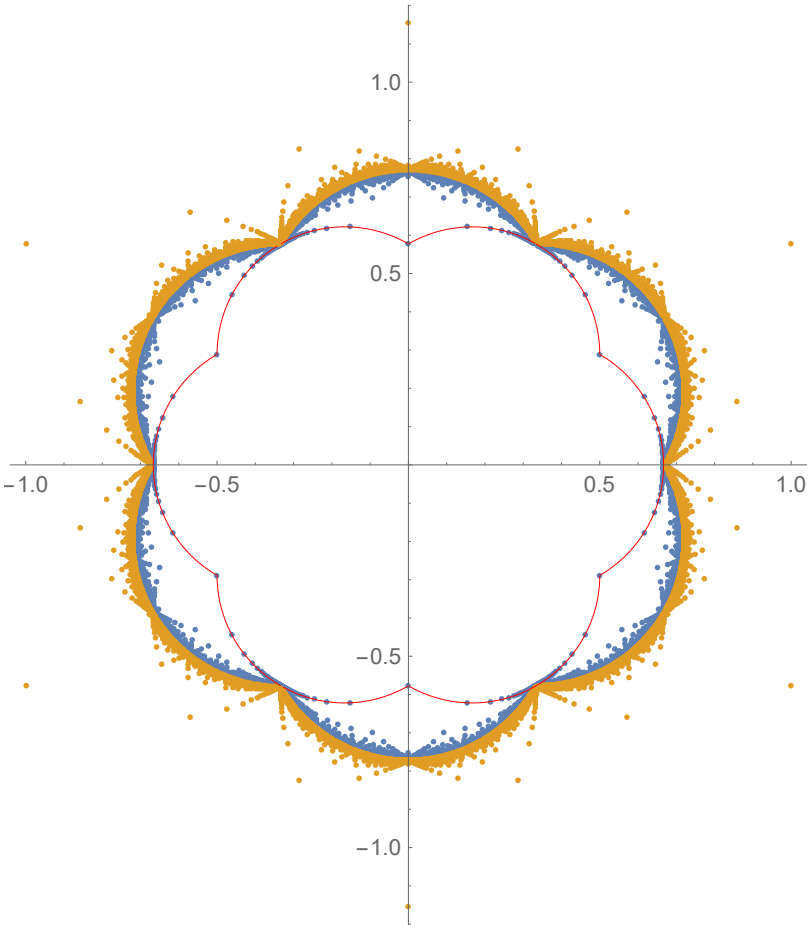


Figure 4.11: The edge energy function of Liu et al. is shown in red and overlaid on the plot of funny edge energies γ.

The lattices are oriented so that the Wulff shapes are both hexagons with the same orientation for easy comparison.

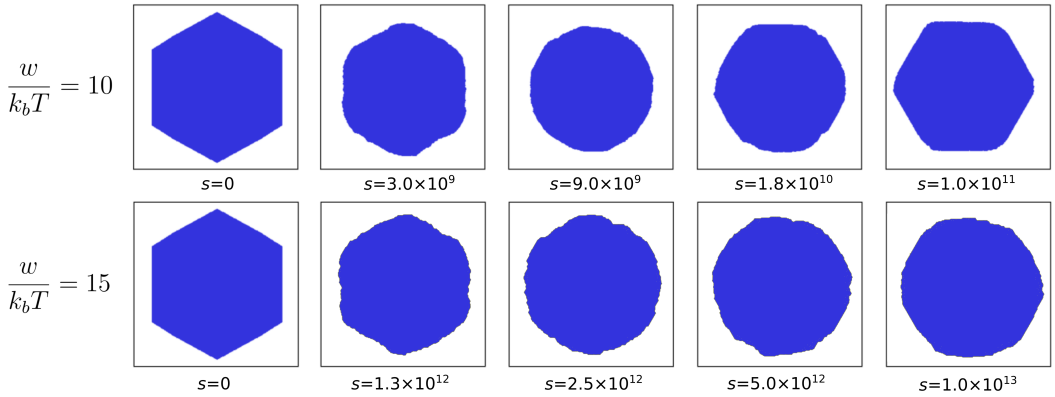


Figure 4.12: Two 2-dimensional KMC simulations with reflective boundary conditions yielding equilibrium shapes. The top row is the time evolution of a flake of material with triangular lattice structure. The bottom row is that of a graphene flake, rotated so that both simulations have identically oriented equilibrium shapes. s is the number of KMC iterations.

There are a couple of critical observations in comparing these two simulations. First, the initial hexagons have the same area, implying that the system size of the triangular simulation is 1.5 times that of the graphene simulation (60,000 vs 40,000), due to there being more nodes in the lattice per area. Next, the equilibrium shape in the graphene simulation is more rounded than the triangular equilibrium shape despite having a greater value for $w/(k_bT)$. Recall from the previous chapter that higher temperature simulation leads to a greater difference between the edge energy and the edge free energy and a rounder equilibrium shape. The effective temperature in this graphene simulation is actually higher than the triangular, because of a smaller set of nearest-neighbor directions leading to less-coordinated atoms.

Normally, a simulation with lower system size and higher temperature should reach equilibrium faster. However, the graphene flake takes a dramatically greater amount of time to reach equilibrium. It is likely that this is a result of the existence of funny directions for graphene. Remember that graphene edge energy in this model

is minimized at a funny direction and note in Fig. 4.8 that in a neighborhood around the zigzag orientation there are no other orientations with an energy value close to that of zigzag. Kinetic Monte Carlo simulations seek lower-energy configurations locally around the current configuration. Without funny directions, this sampling quickly finds lower energy configurations along a continuous edge energy curve. On a non-Bravais lattice however, funny directions give discontinuities in the edge energy which appear to make it harder for the simulation to find lower energy configurations.

4.5 Conclusion

We have demonstrated how to calculate the edge energy for any commensurate graphene edge in a bond-counting model given any set of bonds. The methods used in this paper can be applied to a wide set of 2D and 3D crystal lattices. As new materials are discovered everyday, it is important to be able to calculate edge/surface energies and equilibrium shapes. While there are difficulties that may arise when trying to do this for lattices in general, graphene provides a solid foundation and most of the tools needed to be able to examine any crystal lattice of interest.

We have also observed that a material that assumes a non-Bravais lattice structure may have a fundamental difference of behavior when compared to a Bravais material, at least in the time required to find low energy configurations. There is still much more work to investigate and corroborate this hypothesis.

Chapter 5

More Non-Bravais Lattice Examples

The same techniques used earlier for calculating graphene edge energy can also be used for a wide array of non-Bravais lattices. In this chapter I offer a short list.

5.1 Bravais Alloys

Define a Bravais alloy to be a multi-species material in which all atoms lie on the same Bravais lattice. In other words the atom at each node can be one of a small set of distinct types. Presumably this implies that the strengths of bonds vary between each pair of atom types. Additionally, we require that the alloy is a lattice with a basis as defined in Chapter 2, so that all atoms on the basis Bravais lattice originating from one atom are all of the same type. Note that while the lattice itself may be Bravais, the model can be considered non-Bravais due to the fact that atoms are no longer indistinguishable.

For example, consider the regular triangular Bravais lattice defined by primitive vectors $\mathbf{a}_1 = (0, 1)$ and $\mathbf{a}_2 = (\sqrt{3}/2, 1/2)$. A simple Bravais alloy with three species (A, B, C) can be constructed by placing an A atom at each node of the Bravais lattice

with primitive vectors $\mathbf{a}_1 + \mathbf{a}_2$ and $2\mathbf{a}_2 - \mathbf{a}_1$. Similarly, species B and species C are arranged on the same lattice as species A only offset by the vectors $\mathbf{a}_2$ and $\mathbf{a}_2 - \mathbf{a}_1$ respectively as shown in Fig. 5.1.

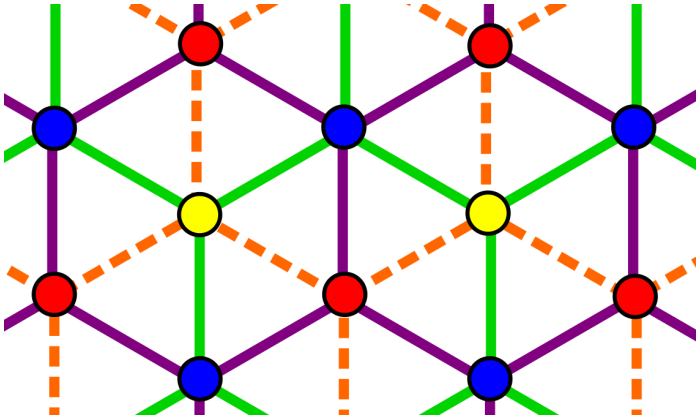


Figure 5.1: An example of a three-species Bravais alloy on the regular triangular lattice. Each species, differentiated by red, yellow and blue nodes, is arrayed in a coarser Bravais lattice. The bonds between each pair of species have a different bond strength indicated by color: orange, green and purple.

In this example there are three different bond strengths of nearest-neighbor bonds; let the strength of a bond between species i and j be denoted w_{ij}. Note that the Bravais lattice formed by all the atoms of a single species is identical to that of all the atoms of one type in the graphene lattice. In fact, mathematically the graphene lattice is a specific instance of this Bravais alloy with atom types treated as the three species and weights $w_{12} = 1$, $w_{13} = 0$ and $w_{23} = 0$.

The set of uniform directions of this alloy is identical to that of graphene, since any facet that passes through both A and B atoms must also pass through C atoms. We observe here that plotting all bonds of weight w_{ij} yields the edges of the graphene lattice offset from those of the other two weights but with the same orientation. Thus the contribution of each bond type to the edge energy of a uniform edge is $\frac{w_{ij}}{3}\Gamma$ and the total uniform edge energy is given by:

$$\gamma(\hat{\mathbf{n}}) = \frac{w_{12} + w_{13} + w_{23}}{3}\Gamma(\hat{\mathbf{n}}).$$

Note that this gives the correct values for the regular triangular lattice ($w_{12} = w_{13} = w_{23} = 1$) as well as the graphene lattice (($w_{12} = 1, w_{13} = w_{23} = 0$).

Funny directions on the alloy are more complicated. Recall the use of bands to calculate funny edge energy in the previous chapter. In the alloy, there are now three categories of bands each with potentially distinct edge energy. Within each band, one of the bond types contributes its thin-band energy value to the energy total and the other two types contribute their thick-band values. Assuming without loss of generality that the bonds contributing graphene thin band value are those between species A and B, the edge energy contribution for a particular bond-direction $\mathbf{v}$ can be written:

$$\gamma_{\mathbf{v}}(\hat{\mathbf{n}}) = \frac{w_{12} + w_{13} + w_{23}}{3}\Gamma_{\mathbf{v}}(\hat{\mathbf{n}}) + \frac{1}{3p}(2w_{12} - w_{13} - w_{23}) \text{ if } b_{\mathbf{v}} \equiv 1 \bmod 3$$

or

$$\gamma_{\mathbf{v}}(\hat{\mathbf{n}}) = \frac{w_{12} + w_{13} + w_{23}}{3}\Gamma_{\mathbf{v}}(\hat{\mathbf{n}}) + \frac{1}{3p}(w_{13} + w_{23} - 2w_{12}) \text{ if } b_{\mathbf{v}} \equiv 2 \bmod 3.$$

Then the total edge energy is calculated by summing over all $\mathbf{v}$.

For example, consider the armchair edge with normal $\hat{\mathbf{n}} = (0, 1)$ on an alloy with weights $w_{12} = 0.5, w_{13} = 1.0$ and $w_{23} = 1.5$. The set of nearest-neighbor bonds is given by $V = \{\mathbf{v}_1 = (0, 1), \mathbf{v}_2 = (\sqrt{3}/2, 1/2), \mathbf{v}_3 = (-\sqrt{3}/2, 1/2)\}$. Then $b_{\mathbf{v}_1} = 2$ and $b_{\mathbf{v}_2} = b_{\mathbf{v}_3} = 1$. Since $\Gamma(\hat{\mathbf{n}}) = 4/\sqrt{3}$, the edge energy in the band in which AB bonds contribute thin band values is given by:

$$\gamma_1(\hat{\mathbf{n}}) = \sum_V \gamma_{\mathbf{v}}(\hat{\mathbf{n}}) = \frac{w_{12} + w_{13} + w_{23}}{3}\Gamma(\hat{\mathbf{n}}) + \frac{1}{3\sqrt{3}}\left[(w_{13} + w_{23} - 2w_{12}) + 2(2w_{12} - w_{13} - w_{23})\right]$$

$$= \Gamma(\hat{\mathbf{n}}) + \frac{1}{3\sqrt{3}}(2w_{12} - w_{13} - w_{23}) = \frac{3.5}{\sqrt{3}}.$$

Similarly,

$$\gamma_2(\hat{\mathbf{n}}) = \Gamma(\hat{\mathbf{n}}) + \frac{1}{3\sqrt{3}}(2w_{13} - w_{12} - w_{23}) = \frac{4}{\sqrt{3}}$$

and

$$\gamma_2(\hat{\mathbf{n}}) = \Gamma(\hat{\mathbf{n}}) + \frac{1}{3\sqrt{3}}(2w_{23} - w_{12} - w_{13}) = \frac{4.5}{\sqrt{3}}.$$

5.2 The Hexagonal Close-Packed Lattice

Recall that the hexagonal close-packed (HCP) lattice is a three-dimensional non-Bravais lattice closely related to the face-centered cubic lattice. Similar to the graphene lattice, there are two sets of nearest-neighbor bond directions, although it is only the neighbor directions between sheets of the triangular lattice that differ.

Calculating the surface energy for an HCP material is very similar to the computation of graphene edge energy. The corresponding Bravais refined lattice can be constructed by placing new nodes at the center of each triangle formed by nearest-neighbor bonds within each sheet of the HCP lattice as shown in Fig. 5.2. Every sheet is a two-dimensional triangonal lattice so each of the bond-directions within a sheet do not have any funny orientations. The calculation of funny facet energies then only depend on the contributions of bonds between sheets of the lattice. The associated bond-lines only coincide with bonds for one sixth of their lengths, yielding

$$\gamma = \frac{1}{6}\Gamma$$

where Γ is the surface energy on the Bravais refined lattice. The remaining work here is to find a set of funny facet orientations with period below some area threshold and calculate the energy values for each.

More non-Bravais lattices with a basis have further complications. Most of these lattices, for example, have more than two atoms within a basis cell. Others have bonds that do not lie on commensurate bond lines. For the most part, these lattices will require case by case inspection to overcome the associated difficulties, although

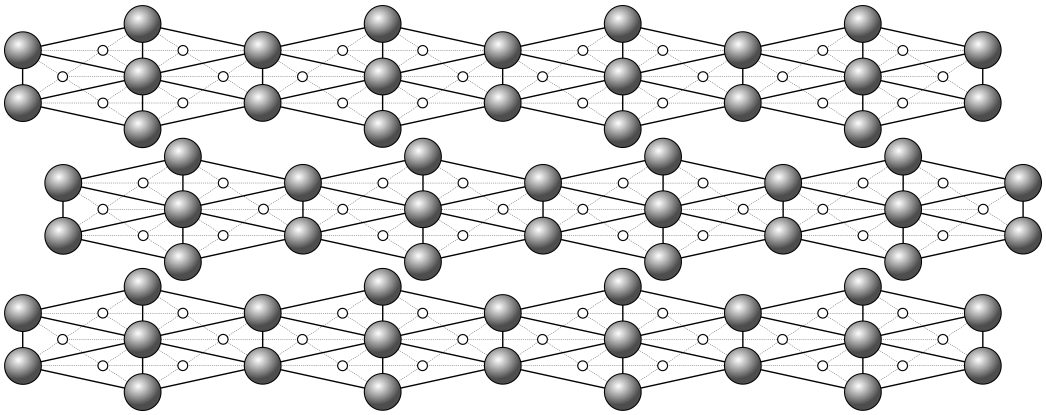


Figure 5.2: The Bravais refined lattice corresponding to the HCP lattice.

there is more work that can be done on calculation of surface energy for this class of lattices in general.

Chapter 6

Conclusion

Within this dissertation are two main results:

1. I have demonstrated that there is an inherent difference in the truncation of surface energy between KMC bond-counting models and continuum crystal growth models. This leads to growth behaviors that may manifest in one model but not the other.

2. I have demonstrated the computation of a discontinuous, multi-valued edge energy function for the graphene lattice and shown that the existence of funny edges may affect graphene growth behavior.

I have also shown areas in which this work can be generalized to more materials with more exotic lattice structures. I plan on continuing this research to build the theory of surface energy calculation and dendritic growth.

These ideas are important to anyone using KMC or other atomistic modelling methods to study crystal growth, as an improved understanding of surface energy lends itself to a greater understanding of growth behavior. However, the methods for calculating surface energy directly from a material's lattice structure can be used to implement atomistic effects in a continuum crystal growth model by informing the choice of surface energy function. In particular, if funny directions do greatly

influence growth behavior, there is work needed to understand how one can introduce this influence into continuum models. Hopefully, the work done here will be expanded upon by myself and others and both continuum and atomistic models will benefit as a result.

Bibliography

C. K. Gan, D. S. (2009). Trends in graphene edge properties and flake shapes: a first-principles study. 35, 49

Davis, S. (2001). *Theory of Solidification*. Cambridge University Press. 30

Fonseca, I. (1991). The wulff theorem revisited. *Proc. Roy. Soc. London A*, 432:125–145. 26

Gh. Jiang, L. Wang, T. C. e. a. (2005). Preparation and characterization of dendritic silver nanoparticles. *J. Mater. Sci.*, 40:1681. 30

Harris, R. and Grant, M. (1990). Monte carlo simulation of a kinetic ising model for dendritic growth. *J. Phys. A: Math. Gen.*, 23:567–571. 17

Herring, C. (1951). Some theorems on the free energies of crystal surfaces. *Phys. Rev.*, 82:87–93. 23

J.J. Hoyt, M. A. and Karma, A. (2003). Atomistic and continuum modeling of dendritic solidification. *Mater. Sci. Eng. R*, 41:121–163. 18, 31

J.K. Mackenzie, A. M. and Nicholas, J. (1962). Bonds broken at atomically flat crystal surfaces i: Face-centered and body-centered cubic crystals. *J. Phys. Chem. Solids*, 23:185–196. 22

L. Jorgenson, R. Harris, M. G. and Guo, H. (1993). Monte carlo simulation studies of dendritic instabilities in three dimensions. *Phys. Rev. E*, 47:1235–1242. 17

O. Shochet, K. Kassner, E. B.-J. S. L. and Muller-Krumbhaar, H. (1992). Morphology transitions during non-equilibrium growth. *Physica A*, 181. 17

P. Branicio, M. Jhon, C. K. G. D. S. (2011). Properties on the edge: graphene edge energies, edge stresses, edge warping, and the wulff shape of graphene flakes. *Modelling and Simul. Mater. Sci. Eng.*, 19. 35

Saito, Y. and Ueta, T. (1989). Monte carlo studies of equilibrium and growth shapes of a crystal. *Phys. Rev. A*, 40:3408–3419. 17

Schulze, T. (2008a). Efficient kinetic monte carlo simulation. *Journal of Computational Physics*, 227:2455–2462. 11

Schulze, T. (2008b). Simulation of dendritic growth into an undercooled melt using kinetic monte carlo techniques. *Physical Review E*, 78(020601). 17

T. Haxhimali, A. Karma, F. G. and Rappaz, M. (2006). Orientation selection in dendritic evolution. *Nature Materials*, 5:660–664. 17, 30, 32

Vicsek, T. (1984). Pattern formation in diffusion-limited aggregation. *Phys. Rev. Lett.*, 53:2281–2284. 17

Voter, A. (2007). Introduction to the kinetic monte carlo method. *Radiation Effects in Solids*, pages 1–23. 19

W. Wang, D. Wang, X. L. Q. P. Y. L. (2013). Pt-ni nanodendrites with high hydrogenation activity. *Chem. Commun.*, 49:2903–2905. 30

Weyl, H. (1916). Ueber die gleichverteilung von zahlen mod. *Math. Ann.*, 77:313–352. 46

Witten, T. and Sander, L. (1981). Diffusion-limited aggregation, a kinetic critical phenomenon. *Phys. Rev. Lett.*, 47. 17

Y. Liu, A. Dobrinsky, B. Y. (2010). Graphene edge from armchair to zigzag: The origins of nanotube chirality? *Phys. Rev. Lett.*, 105. 35, 49

Y. Luo, R. Q. (2014). Influences of the third and fourth nearest neighboring interactions on the surface anisotropy of face-centered-cubic metals. *Surface Science*, 624:103–111. 22

Vita

Tim Krumwiede was born in Provo, UT to Kip and Lana Krumwiede and is the oldest of four children. After moving several times during childhood, he graduated with the class of 2004 from Boise High School in Boise, ID. He then attended Brigham Young University in Utah for one year before taking a couple years away from school to serve as a missionary for the Church of Jesus Christ of Latter-Day Saints in the country of Albania. Upon returning, Tim resumed his education at BYU and graduated with a Bachelors of Science in 2011 majoring in mathematics. During this time, he participated in two undergraduate research projects: one on odd perfect numbers and another on mathematical models of mosquito populations. Upon graduation, he started as a graduate student in mathematics at the University of Tennessee. After one semester without funding, Tim received a graduate teaching assistantship from the math department. He began to do research on mathematical models of crystal growth under Dr. Tim Schulze. Tim defended his dissertation in November of 2016 and finished his degree in the fall of that year.